

Beyond Born-Oppenheimer Based Diabatic Surfaces of $1,3,5\text{-C}_6\text{H}_3\text{F}_3^+$ to Generate the Photoelectron Spectra Using Time-Dependent Discrete Variable Representation Approach

Soumya Mukherjee^{a,1}, Satyam Ravi^{a,b,1}, Joy Dutta^a, Subhankar Sardar^c and Satrajit Adhikari^{a,*}

^aSchool of Chemical Sciences,

Indian Association for the Cultivation of Science, Jadavpur, Kolkata - 700032, India

^bSchool of Advance Science and Languages, VIT Bhopal University, Bhopal - 466114, India

^cDepartment of Chemistry, Bhatter College, Dantan, Paschim Medinipur - 721426, India

Electronic Supplementary Information

* Author for correspondence: e-mail: pcsa@iacs.res.in

¹S. Mukherjee and S. Ravi contributed equally to this work

S1 Adiabatic to Diabatic Transformation (ADT) equations for six (6) electronic state Sub-Hilbert space¹

For six (6) coupled electronic manifold, the model ADT matrix can be constructed by multiplying fifteen (15) elementary rotation matrices in $15!$ ways, but in the present calculation, we adopt the following order:

$$\mathbf{A} = \mathbf{A}^{12}(\Theta_{12}) \cdot \mathbf{A}^{13}(\Theta_{13}) \cdot \mathbf{A}^{23}(\Theta_{23}) \cdot \mathbf{A}^{14}(\Theta_{14}) \cdot \mathbf{A}^{24}(\Theta_{24}) \cdot \mathbf{A}^{34}(\Theta_{34}) \cdot \mathbf{A}^{15}(\Theta_{15}) \cdot \mathbf{A}^{25}(\Theta_{25}) \cdot \mathbf{A}^{35}(\Theta_{35}) \cdot \mathbf{A}^{45}(\Theta_{45}) \cdot \mathbf{A}^{16}(\Theta_{16}) \cdot \mathbf{A}^{26}(\Theta_{26}) \cdot \mathbf{A}^{36}(\Theta_{36}) \cdot \mathbf{A}^{46}(\Theta_{46}) \cdot \mathbf{A}^{56}(\Theta_{56}),$$

where Θ s are the ADT angles. Since most of the ADT equations for six (6) electronic states are large and complicated, we present some representative ADT equations as follows:

$$\begin{aligned} \vec{\nabla}\Theta_{12} = & -\vec{\tau}_{12} - \sin\Theta_{12}\tan\Theta_{13}\vec{\tau}_{13} - \cos\Theta_{12}\tan\Theta_{13}\vec{\tau}_{23} - \sin\Theta_{12}\sec\Theta_{13}\tan\Theta_{14}\vec{\tau}_{14} - \cos\Theta_{12}\sec\Theta_{13}\tan\Theta_{14}\vec{\tau}_{24} \\ & - \sin\Theta_{12}\sec\Theta_{13}\sec\Theta_{14}\tan\Theta_{15}\vec{\tau}_{15} - \cos\Theta_{12}\sec\Theta_{13}\sec\Theta_{14}\tan\Theta_{15}\vec{\tau}_{25} \\ & - \sin\Theta_{12}\sec\Theta_{13}\sec\Theta_{14}\sec\Theta_{15}\tan\Theta_{16}\vec{\tau}_{16} - \cos\Theta_{12}\sec\Theta_{13}\sec\Theta_{14}\sec\Theta_{15}\tan\Theta_{16}\vec{\tau}_{26} \end{aligned} \quad (1a)$$

$$\begin{aligned} \vec{\nabla}\Theta_{13} = & -\cos\Theta_{12}\vec{\tau}_{13} + \sin\Theta_{12}\vec{\tau}_{23} - \cos\Theta_{12}\sin\Theta_{13}\tan\Theta_{14}\vec{\tau}_{14} + \sin\Theta_{12}\sin\Theta_{13}\tan\Theta_{14}\vec{\tau}_{24} - \cos\Theta_{13}\tan\Theta_{14}\vec{\tau}_{34} \\ & - \cos\Theta_{12}\sin\Theta_{13}\sec\Theta_{14}\tan\Theta_{15}\vec{\tau}_{15} + \sin\Theta_{12}\sin\Theta_{13}\sec\Theta_{14}\tan\Theta_{15}\vec{\tau}_{25} - \cos\Theta_{13}\sec\Theta_{14}\tan\Theta_{15}\vec{\tau}_{35} \\ & - \cos\Theta_{12}\sin\Theta_{13}\sec\Theta_{14}\sec\Theta_{15}\tan\Theta_{16}\vec{\tau}_{16} + \sin\Theta_{12}\sin\Theta_{13}\sec\Theta_{14}\sec\Theta_{15}\tan\Theta_{16}\vec{\tau}_{26} \\ & - \cos\Theta_{13}\sec\Theta_{14}\sec\Theta_{15}\tan\Theta_{16}\vec{\tau}_{36} \end{aligned} \quad (1b)$$

$$\begin{aligned} \vec{\nabla}\Theta_{14} = & -\cos\Theta_{12}\cos\Theta_{13}\vec{\tau}_{14} + \sin\Theta_{12}\cos\Theta_{13}\vec{\tau}_{24} + \sin\Theta_{13}\vec{\tau}_{34} - \cos\Theta_{12}\cos\Theta_{13}\sin\Theta_{14}\tan\Theta_{15}\vec{\tau}_{15} \\ & + \sin\Theta_{12}\cos\Theta_{13}\sin\Theta_{14}\tan\Theta_{15}\vec{\tau}_{25} + \sin\Theta_{13}\sin\Theta_{14}\tan\Theta_{15}\vec{\tau}_{35} - \cos\Theta_{14}\tan\Theta_{15}\vec{\tau}_{45} \\ & - \cos\Theta_{12}\cos\Theta_{13}\sin\Theta_{14}\sec\Theta_{15}\tan\Theta_{16}\vec{\tau}_{16} + \sin\Theta_{12}\cos\Theta_{13}\sin\Theta_{14}\sec\Theta_{15}\tan\Theta_{16}\vec{\tau}_{26} \\ & + \sin\Theta_{13}\sin\Theta_{14}\sec\Theta_{15}\tan\Theta_{16}\vec{\tau}_{36} - \cos\Theta_{14}\sec\Theta_{15}\tan\Theta_{16}\vec{\tau}_{46} \end{aligned} \quad (1c)$$

$$\begin{aligned} \vec{\nabla}\Theta_{15} = & -\cos\Theta_{12}\cos\Theta_{13}\cos\Theta_{14}\vec{\tau}_{15} + \sin\Theta_{12}\cos\Theta_{13}\cos\Theta_{14}\vec{\tau}_{25} + \sin\Theta_{13}\cos\Theta_{14}\vec{\tau}_{35} + \sin\Theta_{14}\vec{\tau}_{45} \\ & - \cos\Theta_{12}\cos\Theta_{13}\cos\Theta_{14}\sin\Theta_{15}\tan\Theta_{16}\vec{\tau}_{16} + \sin\Theta_{12}\cos\Theta_{13}\cos\Theta_{14}\sin\Theta_{15}\tan\Theta_{16}\vec{\tau}_{26} \\ & + \sin\Theta_{13}\cos\Theta_{14}\sin\Theta_{15}\tan\Theta_{16}\vec{\tau}_{36} + \sin\Theta_{14}\sin\Theta_{15}\tan\Theta_{16}\vec{\tau}_{46} - \cos\Theta_{15}\tan\Theta_{16}\vec{\tau}_{56} \end{aligned} \quad (1d)$$

$$\begin{aligned} \vec{\nabla}\Theta_{16} = & -\cos\Theta_{12}\cos\Theta_{13}\cos\Theta_{14}\cos\Theta_{15}\vec{\tau}_{16} + \sin\Theta_{12}\cos\Theta_{13}\cos\Theta_{14}\cos\Theta_{15}\vec{\tau}_{26} + \sin\Theta_{13}\cos\Theta_{14}\cos\Theta_{15}\vec{\tau}_{36} \\ & + \sin\Theta_{14}\cos\Theta_{15}\vec{\tau}_{46} + \sin\Theta_{15}\vec{\tau}_{56} \end{aligned} \quad (1e)$$

S2 Path Dependence of Diabatic Potential Energy Surfaces (PESSs) Matrix

S2.1 Theoretical Background

It is evident from Eqs. 9 and 11 of the main text that the ADT equations involve skew-symmetric nonadiabatic coupling matrix (τ), which is non-Abelian for N (≥ 3) dimensional sub-Hilbert space. Hence, the solution of those coupled differential equations depends on the choice of contour on a two-dimensional (2D) nuclear plane. As for example, for a system with two nuclear coordinates p and q , we consider two different paths with same initial and final nuclear coordinates (p_0, q_0 to $p_0 + \Delta p, q_0 + \Delta q$, see Fig. S1) and the resulting integral form of ADT matrix equations are:

$$A_1 = A(p_0 + \Delta p, q_0 + \Delta q) = \exp \left(- \int_{q_0}^{q_0 + \Delta q} \tau_q(p_0 + \Delta p, q) dq - \int_{p_0}^{p_0 + \Delta p} \tau_p(p, q_0) dp \right) A(p_0, q_0) \quad (2a)$$

$$A_2 = A(p_0 + \Delta p, q_0 + \Delta q) = \exp \left(- \int_{p_0}^{p_0 + \Delta p} \tau_p(p, q_0 + \Delta q) dp - \int_{q_0}^{q_0 + \Delta q} \tau_q(p_0, q) dq \right) A(p_0, q_0), \quad (2b)$$

and their product takes the following form:²

$$A_1^\dagger A_2 = A^\dagger(p_0, q_0) \exp(-\Delta p \Delta q (\text{curl}^{pq} \tau)) A(p_0, q_0), \quad (3)$$

where $\text{curl}^{pq} \tau \left[= \left(\frac{\partial \tau_p}{\partial q} - \frac{\partial \tau_q}{\partial p} \right)_{(\bar{p}, \bar{q})} \right]$, \bar{p} and \bar{q} represent the midpoints of p_0 and $p_0 + \Delta p$, and q_0 and $q_0 + \Delta q$, respectively symbolize the component of $\text{curl } \tau$ over the $p - q$ nuclear plane. Fig. S1 shows that $A_1(p_0 + \Delta p, q_0 + \Delta q)$ and $A_2(p_0 + \Delta p, q_0 + \Delta q)$ are the two ADT matrices obtained along two different paths of integration.

On the other hand, the ADT matrix at the initial geometry ($A(p_0, q_0)$) being an orthogonal matrix could be considered as a unit one. In case of two state sub-Hilbert space, $\text{curl}^{pq} \tau$ is always zero and therefore, the two matrices, A_1 and A_2 are identical (see Eq. 3). On the contrary, for non-Abelian cases ($N \geq 3$), $\text{curl}^{pq} \tau$ is nonzero, but the product matrix ($B = A_1^\dagger A_2$) appears as an orthogonal one:

$$\begin{aligned} B^\dagger B &= A^\dagger(p_0, q_0) \exp(\Delta p \Delta q (\text{curl}^{pq} \tau)) A(p_0, q_0) A^\dagger(p_0, q_0) \exp(-\Delta p \Delta q (\text{curl}^{pq} \tau)) A(p_0, q_0) \\ &= I, \end{aligned} \quad (4)$$

which clearly indicates that any two ADT matrices (A_1 and A_2) calculated along two different paths over the nuclear configuration space (CS) are related through an orthogonal transformation

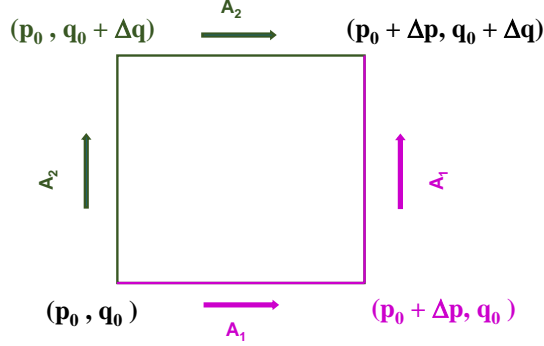


FIG. S1: Two different paths of integration for ADT matrix (A) are displayed with same initial (p_0, q_0) and final $(p_0 + \Delta p, q_0 + \Delta q)$ nuclear configurations, where two different solutions (A_1 and A_2) are obtained for non-Abelian nonadiabatic coupling matrix ($N \geq 3$).

(B).

Alternatively, two different ADT matrices (A_1 and A_2) along two different paths ending at the same point $(p_0 + \Delta p, q_0 + \Delta q)$ will provide the following diabatic PESs matrices:

$$W_1 = A_1^\dagger U A_1 \quad \text{and} \quad W_2 = A_2^\dagger U A_2, \quad (5)$$

which leads to

$$A_1 W_1 A_1^\dagger = A_2 W_2 A_2^\dagger = U \quad (6)$$

arriving

$$W_1 = B W_2 B^\dagger. \quad (7)$$

Since $B (= A_1^\dagger A_2)$ is also an orthogonal matrix (see Eq. 4), the above equation affirms the path independence of calculated observables obtained from different diabatic matrices (W_1 and W_2).²⁻⁴

Moreover, it should be clearly mentioned that for three or more than three nuclear degrees of freedom (DOFs), the contour integration needs to be carried out on a set of 2D cross sections of the original higher dimensional nuclear space.^{3,5,6}

S2.2 Paths of Integration in ADT Calculation of 1,3,5-C₆H₃F₃⁺ (TFBz⁺)

While performing the adiabatic-to-diabatic transformation, *ab initio* calculated ρ and ϕ components (polar counterparts of any normal mode pair) of nonadiabatic coupling terms (NACTs) are substituted in Eq. 11 of the main text and those stiff coupled differential (ADT) equations are numerically solved by backward differentiation formula (BDF) over the ρ - ϕ planes with reasonable relative and absolute error tolerance. In our study, we opt two rectangular paths of integration (see Fig S2), where (a) path I is used to extract the information of conical intersection(s) [CI(s)]/seam(s) by analysing the profiles of ADT angles and sign inversion of ADT matrix elements, and (b) path II is employed to calculate the diabatic PES matrix for quantum dynamical calculations. While choosing path I, the ADT equations need to be solved along the ρ coordinate from ρ_{max} to ρ_{min} at $\phi = \phi_{min} (= 0)$ and then, considering the ADT angles at each grid of ρ as the initial values, those equations are further solved along the ϕ grid from 0 to 2π . On the other hand, in path II, initially numerical calculation is performed along ϕ coordinate from 0 to 2π at fixed ρ ($= \rho_{min}$) followed by integration along ρ coordinate for each and every value of ϕ .

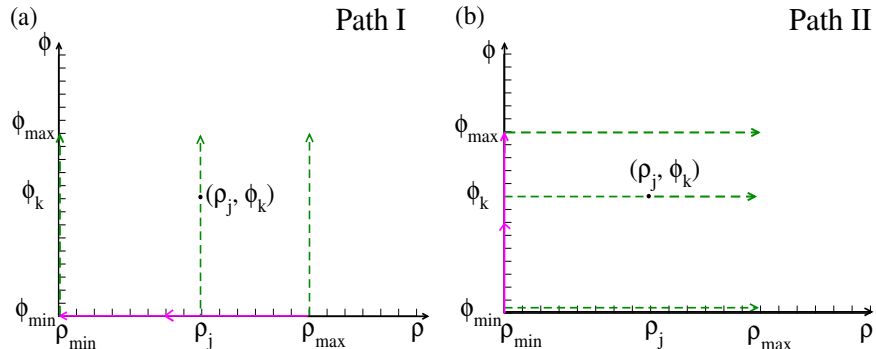


FIG. S2: Diagram (a) and (b) depict two paths of integration along which the ADT equations are numerically solved. For each case, the ADT equations are first solved along the bold magenta line and then, along the dotted green lines.

S3 Explicit Form of Time Dependent Discrete Variable Representation (TDDVR) Matrix Equation for Quantum Motion^{4,7}

One can write the time dependence of TDDVR coefficients ($d_{i_1 i_2 \dots i_p, l}$) in the following form:

$$\begin{aligned}
i\hbar \dot{d}_{i_1 i_2 \dots i_p, l} &= \frac{1}{2} \left\{ \sum_k \dot{p}_{Q_k^c} \sqrt{\frac{\hbar}{ImA^k}} \bar{X}_{i_k i_k}^k \right\} d_{i_1 i_2 \dots i_p, l} + \left\{ \sum_k \frac{\mu(\dot{s}_c^k)^2}{2} \right\} d_{i_1 i_2 \dots i_p, l} \\
&+ W_{ll}(i_1 i_2 \dots i_p) d_{i_1 i_2 \dots i_p, l} + \sum_{l' \neq l} W_{ll'}(i_1 i_2 \dots i_p) d_{i_1 i_2 \dots i_p, l'} \\
&+ \sum_k \left\{ \frac{\hbar ImA^k}{2\mu} \sum_{i'_1 i'_2 \dots i'_p} \bar{Y}_{i_k i'_k}^k d_{i'_1 i'_2 \dots i'_p, l} \prod_{k' \neq k} \delta_{i_{k'} i'_{k'}} \right\}, \tag{8}
\end{aligned}$$

where

$$\begin{aligned}
\bar{X}_{i_k, i'_k}^k &= \frac{X_{i_k, i'_k}^k}{\sqrt{A_{i_k, i_k}^k A_{i'_k, i'_k}^k}}, \quad \bar{Y}_{i_k, i'_k}^k = \frac{Y_{i_k, i'_k}^k}{\sqrt{A_{i_k, i_k}^k A_{i'_k, i'_k}^k}} = \frac{2E_{i_k, i'_k}^k - F_{i_k, i'_k}^k}{\sqrt{A_{i_k, i_k}^k A_{i'_k, i'_k}^k}} \\
d_{i_1 i_2 \dots i_p, l} &= c_{i_1 i_2 \dots i_p, l} \prod_{k=1}^p (A_{i_k, i_k}^k)^{\frac{1}{2}}, \\
A_{i_k, i'_k}^k &= \sum_{n=0}^{N^k} \zeta_n^*(x_{i_k}^k) \zeta_n(x_{i'_k}^k), \\
X_{i_k, i'_k}^k &= \sum_{n=0}^{N^k-1} \zeta_{n+1}^*(x_{i_k}^k) \sqrt{n+1} \zeta_n(x_{i'_k}^k) + \sum_{n=1}^{N^k} \zeta_{n-1}^*(x_{i_k}^k) \sqrt{n} \zeta_n(x_{i'_k}^k), \\
E_{i_k, i'_k}^k &= \sum_{n=0}^{N^k} \zeta_n^*(x_{i_k}^k) 2n \zeta_n(x_{i'_k}^k), \\
F_{i_k, i'_k}^k &= \sum_{n=0}^{N^k-2} \zeta_{n+2}^*(x_{i_k}^k) \sqrt{(n+1)(n+2)} \zeta_n(x_{i'_k}^k) + \sum_{n=2}^{N^k} \zeta_{n-2}^*(x_{i_k}^k) \sqrt{n(n-1)} \zeta_n(x_{i'_k}^k) \\
&+ \sum_{n=0}^{N^k} \zeta_n^*(x_{i_k}^k) (2n+1) \zeta_n(x_{i'_k}^k)
\end{aligned}$$

The other symbols [W_{ll} , $\zeta_n(x_{i_k}^k)$, ...] are already specified in the main text. It is important to mention that the time-independent component matrices ($\{\mathbf{A}^k\}$, $\{\mathbf{X}^k\}$, $\{\mathbf{E}^k\}$, $\{\mathbf{F}^k\}$) of the TDDVR Hamiltonian matrix (Eq. 8) are calculated only once during the dynamical calculations. Since the diagonal elements of the matrix, $\{\mathbf{X}^k\}$ are multiplied with the “classical” variables, $\{\dot{p}_{Q_k^c}(t)\}$, the

quantum equations of motion (Eq. 8) are free from any nonlinear contribution due to “classical” equation. On the contrary, the full matrices, $\{\mathbf{E}^k\}$ and $\{\mathbf{F}^k\}$ incorporate the couplings among the grid-points (see Eq. 8). Since matrix ($\{\mathbf{E}^k\}$ and $\{\mathbf{F}^k\}$) vector (\mathbf{d}) multiplication can be done independent from one mode to other, parallel computation can be used to find the numerical solution of the differential equation (Eq. 8). Such extensive parallel computation has successfully reduced the computational cost even for large dimensional spectroscopic systems.

S4 Expressions of Classical Path Equations in TDDVR Formalism

In TDDVR methodology, the classical path equations for the k^{th} mode take the following forms:

$$\dot{Q}_k^c(t) = \frac{p_{Q_k^c}(t)}{\mu}, \quad (9)$$

$$\dot{p}_{Q_k^c}(t) = -\frac{dW(\{Q_k\})}{dQ_k} \Big|_{Q_k(t)=Q_k^c(t)}. \quad (10)$$

While implementing Dirac-Frenkel variational principle,⁸ we achieve the rigorous expression of $\dot{p}_{Q_k^c}$ for multi-mode multi-surface spectroscopic systems by minimizing the following integral:

$$\begin{aligned} I &= \int \left(-i\hbar \frac{\partial \Xi^*(\{Q_k\}, t)}{\partial t} - H(\{p_{Q_k}\}, \{Q_k\}) \Xi^*(\{Q_k\}, t) \right) \\ &\times \left(i\hbar \frac{\partial \Xi(\{Q_k\}, t)}{\partial t} - H(\{p_{Q_k}\}, \{Q_k\}) \Xi(\{Q_k\}, t) \right) \prod_{k=1}^p dQ_k, \end{aligned} \quad (11)$$

with respect to $\{\dot{p}_{Q_k^c}\}$. The explicit expression of $\{\dot{p}_{Q_k^c}\}$ is as follows:

$$\begin{aligned}
\dot{p}_{Q_k^c}(t) &= \left[\frac{2(ImA^k)^2}{\mu} \left\{ \sum_l \sum_{i_k i'_k} c_{i_1 i_2 .. i_k .. i_p, l}^*(t) \frac{\sum_{i''_k} c_{i_1 i_2 .. i''_k .. i_p, l}(t) S_{i''_k i'_k}^{(2)}}{A_{i'_k i'_k}} S_{i_k i'_k}^{*(1)} \right. \right. \\
&+ \sum_l \sum_{i_k i'_k} \frac{\sum_{i''_k} c_{i_1 i_2 .. i''_k .. i_p, l}^*(t) S_{i''_k i'_k}^{(2)}}{A_{i_k i_k}} c_{i_1 i_2 .. i'_k .. i_p, l}(t) S_{i_k i'_k}^{*(1)} \\
&- 2 \sum_l \sum_{i_k i'_k} c_{i_1 i_2 .. i_k .. i_p, l}^*(t) c_{i_1 i_2 .. i'_k .. i_p, l}(t) S_{i_k i'_k}^{*(3)} \Big\} \\
&- \frac{\hbar Im A^k}{\mu} \left\{ \sum_l \sum_{i_k i'_k} c_{i_1 i_2 .. i_k .. i_p, l}^*(t) \frac{\sum_{i''_k} c_{i_1 i_2 .. i''_k .. i_p, l}(t) R_{i''_k i'_k}}{A_{i'_k i'_k}} S_{i_k i'_k}^{*(1)} \right. \\
&+ \sum_l \sum_{i_k i'_k} \frac{\sum_{i''_k} c_{i_1 i_2 .. i''_k .. i_p, l}^*(t) R_{i''_k i'_k}}{A_{i_k i_k}} c_{i_1 i_2 .. i'_k .. i_p, l}(t) S_{i_k i'_k}^{*(1)} \\
&- 2 \sum_l \sum_{i_k i'_k} c_{i_1 i_2 .. i_k .. i_p, l}^*(t) c_{i_1 i_2 .. i'_k .. i_p, l}(t) T_{i_k i'_k}^* \Big\} \Big] \\
&\left/ \left[\sum_l \sum_{i_k i'_k} c_{i_1 i_2 .. i_k .. i_p, l}^*(t) \frac{\sum_{i''_k} c_{i_1 i_2 .. i''_k .. i_p}(t) S_{i''_k i'_k}^{(1)}}{A_{i'_k i'_k}} S_{i_k i'_k}^{*(1)} \right. \right. \\
&+ \sum_l \sum_{i_k i'_k} \frac{\sum_{i''_k} c_{i_1 i_2 .. i''_k .. i_p, l}^*(t) S_{i''_k i'_k}^{(1)}}{A_{i_k i_k}} c_{i_1 i_2 .. i'_k .. i_p, l}(t) S_{i_k i'_k}^{*(1)} \\
&- 2 \sum_l \sum_{i_k i'_k} c_{i_1 i_2 .. i_k .. i_p, l}^*(t) c_{i_1 i_2 .. i'_k .. i_p, l}(t) S_{i_k i'_k}^{*(2)} \Big] \right] \quad (12)
\end{aligned}$$

where

$$\begin{aligned}
R_{i_k i'_k} &= \sum_p \zeta_p^*(x_{i_k}^k) \zeta_p(x_{i'_k}^k) 2p \\
S_{i_k i'_k}^{(n)} &= \sum_{pq} \zeta_p^*(x_{i_k}^k) \zeta_q(x_{i'_k}^k) \int \Phi_q^*(Q_k, t) (Q_k - Q_k^c(t))^n \Phi_p(Q_k, t) dQ_k \\
T_{i_k i'_k} &= \sum_{pq} \zeta_p(x_{i_k}^k) \zeta_q^*(x_{i'_k}^k) 2p \int \Phi_p^*(Q_k, t) (Q_k - Q_k^c(t)) \Phi_q(Q_k, t) dQ_k \quad (13)
\end{aligned}$$

with

$$\begin{aligned}
\int \Phi_p^*(Q_k, t)(Q_k - Q_k^c(t))\Phi_q(Q_k, t)dQ_k &= \frac{1}{2}\sqrt{\frac{\hbar}{ImA^k}}\left\{\sqrt{p+1}\delta_{p+1,q} + \sqrt{p}\delta_{p-1,q}\right\} \\
\int \Phi_p^*(Q_k, t)(Q_k - Q_k^c(t))^2\Phi_q(Q_k, t)dQ_k &= \frac{\hbar}{4ImA^k}\left\{\sqrt{(p+1)(p+2)}\delta_{p+2,q}\right. \\
&\quad \left.+ (2p+1)\delta_{p,q} + \sqrt{p(p-1)}\delta_{p-2,q}\right\} \\
\int \Phi_p^*(Q_k, t)(Q_k - Q_k^c(t))^3\Phi_q(Q_k, t)dQ_k &= \frac{1}{8}\left(\frac{\hbar}{ImA^k}\right)^{3/2}\left\{\sqrt{(p+1)(p+2)(p+3)}\delta_{p+3,q}\right. \\
&\quad \left.+ 3(p+1)\sqrt{p+1}\delta_{p+1,q} + 3p\sqrt{p}\delta_{p-1,q}\right. \\
&\quad \left.+\sqrt{p(p-1)(p-2)}\delta_{p-3,q}\right\}
\end{aligned} \tag{14}$$

The matrices, R , $S^{(n)}$, T and A in Eq. (12) are time-independent and thereby, they are computed only once during the dynamical calculation. On the other hand, time-dependence of $\dot{p}_{Q_k^c}$ appears due to the time-dependent coefficient $\{c_{i_1 i_2 \dots i_k \dots i_p, l}(t)\}$. One can further simplify the form of $\dot{p}_{Q_k^c}$ in Eq. (12), if $S_{i_k i'_k}^{(1)}$ is replaced by $S_{i_k i'_k}^{(1)} \delta_{i_k i'_k}$ as the first order term $(Q_k - Q_k^c(t))$ is diagonal in DVR formulation:⁹

$$\begin{aligned}
\dot{p}_{Q_k^c}(t) &= \sum_l \sum_{i_k i'_k} c_{i_1 i_2 \dots i_k \dots i_p, l}^*(t) c_{i_1 i_2 \dots i'_k \dots i_p, l}(t) \\
&\times \left\{ \frac{2(ImA^k)^2}{\mu} \left[S_{i_k i'_k}^{(2)} \frac{{S^{(1)}}_{i_k i_k}^*}{A_{i_k i_k}} - S_{i_k i'_k}^{(3)} \right] - \frac{\hbar ImA^k}{\mu} \left[R_{i_k i'_k} \frac{{S^{(1)}}_{i_k i_k}^*}{A_{i_k i_k}} - T_{i_k i'_k}^* \right] \right\} \\
&/ \left[\sum_l \sum_{i_k} c_{i_1 i_2 \dots i_k \dots i_p, l}^*(t) c_{i_1 i_2 \dots i_k \dots i_p, l}(t) \frac{{S^{(1)}}_{i_k i_k}^* S_{i_k i_k}^{(1)}}{A_{i_k i_k}} \right. \\
&- \left. \sum_l \sum_{i_k i'_k} c_{i_1 i_2 \dots i_k \dots i_p, l}^*(t) c_{i_1 i_2 \dots i'_k \dots i_p, l}(t) S_{i_k i'_k}^{(2)} \right].
\end{aligned} \tag{15}$$

At initial point ($t = 0$), the denominator of Eq. 15 is very small leading to large “quantum force”, which results into numerical inaccuracies in “classical” variables (see Eq. 9 and 15) vis-á-vis quantum equation of motion (see Eq. 8). In order to overcome such difficulties, the “classical” equation of motion needs to be propagated in Newtonian sense (see Eq. 9 and Eq. 10) until the amplitudes of the wavefunction are properly distributed over the expansion coefficient ($\{c_{i_1 i_2 \dots i_k \dots i_p, l}(t)\}$). Once such distribution is achieved, nuclear dynamics can be performed using the quantum force as presented in Eq. 15.

S5 Initialization and Propagation in TDDVR Dynamics

In order to perform TDDVR dynamics, a product of Gaussian functions ($\{\Phi_{GWP}(Q_k)\}$) around the equilibrium geometry ($\{\mathbf{Q}_0\} = \mathbf{0}$) is assumed as the starting wavefunction on a particular electronic state:

$$\prod_{k=1}^p \Phi_{GWP}(Q_k) = \sum_{i_1 i_2 \dots i_p} c_{i_1 i_2 \dots i_p, l} \prod_{k=1}^p \sum_{n=0}^{N_k} \zeta_n^*(x_{i_k}) \Phi_n(Q_k, t). \quad (16)$$

Using the orthogonal property of TDDVR basis at the DVR grid points, we arrive at the following form:

$$\prod_{k=1}^p \Phi_{GWP}(Q_{i_k}) = c_{i_1 i_2 \dots i_p, l} \prod_{k=1}^p \phi(Q_k, t) \sum_{n=0}^{N_k} \zeta_n^*(x_{i_k}) \zeta_n(x_{i_k}), \quad (17)$$

which turns into:

$$\phi^*(Q_k, t) \prod_{k=1}^p \Phi_{GWP}(Q_{i_k}) = c_{i_1 i_2 \dots i_p, l} \prod_{k=1}^p \sum_{n=0}^{N_k} \zeta_n^*(x_{i_k}^k) \zeta_n(x_{i_k}^k) = c_{i_1 i_2 \dots i_p, l} \prod_{k=1}^p A_{i_k i_k}, \quad (18)$$

defining

$$d_{i_1 i_2 \dots i_p, n} = c_{i_1 i_2 \dots i_p, n} \sqrt{\prod_{k=1}^p A_{i_k i_k}} = \frac{\prod_{k=1}^p \zeta_0(x_{i_k})}{\sqrt{\prod_{k=1}^p A_{i_k i_k}}}. \quad (19)$$

Thus, the amplitudes on different surfaces (l) can be expressed with the following column vector,

$$\begin{pmatrix} \mathbf{d}_1(\mathbf{t}) \\ \mathbf{d}_2(\mathbf{t}) \\ \vdots \\ \mathbf{d}_l(\mathbf{t}) \end{pmatrix} \quad (20)$$

On the other hand, the expansion coefficient vectors ($d_{i_1 i_2 \dots i_p, l}$, where $l \neq n$) on other surfaces are initially zero:

$$\dots, d_{i_1 i_2 \dots i_p, n-1}(t=0) = 0, \quad d_{i_1 i_2 \dots i_p, n+1}(t=0) = 0 \dots. \quad (21)$$

After initialization of the wavefunction, the set of differential equations (Eqs. 8 to 10) are solved simultaneously to compute the \mathbf{d} vectors at all the grid-points at each time, t . Once the magnitudes of those vectors are in hand at a specific time t , we perform the following grid-summation to evaluate the probability of finding the system on a specific diabatic surface,

$$P_l^{dia}(t) = \sum_{i_1 i_2 \dots i_p} |d_{i_1 i_2 \dots i_p, l}(t)|^2, l = 1, 2, \dots 6, \quad (22)$$

where the expression of adiabatic population takes the following form,

$$P_l^{adia}(t) = \sum_{i_1 i_2 \dots i_p} |d_{i_1 i_2 \dots i_p, l}^{adia}(t)|^2, l = 1, 2, \dots 6, \quad (23)$$

$$\begin{pmatrix} d_1^{adia}(t) \\ d_2^{adia}(t) \\ \vdots \\ d_6^{adia}(t) \end{pmatrix} = A \cdot \begin{pmatrix} d_1(t) \\ d_2(t) \\ \vdots \\ d_6(t) \end{pmatrix}, \quad (24)$$

by using the ADT matrix, A (see Eq. 10 in main text).

S6 Optimized Parameters of 1,3,5-C₆H₃F₃ (TFBz) Molecule¹

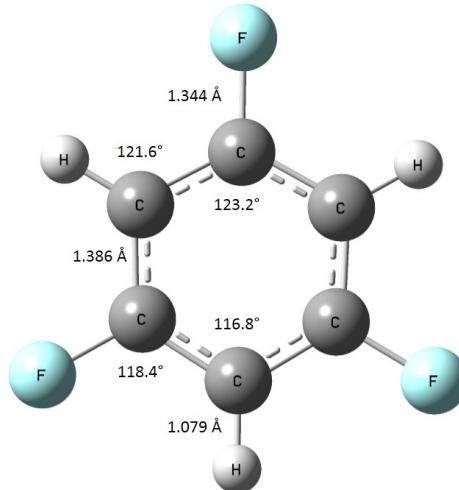


FIG. S3: The TFBz molecule is optimized using MP2 level of electronic structure calculation employing cc-pVDZ basis set. The optimized geometry parameters (bond lengths and bond angles) are specified in the figure and also, in Table S1.

TABLE S1: Equilibrium geometry parameters of TFBz molecule obtained from MP2 methodology employing cc-pVDZ basis set and their comparison with other theoretical findings and experimental data

Parameters	Optimization Result (MP2/cc-pVDZ) ^a	Optimization Result (MP2/cc-pVTZ) ^b	Experimental Result ^c
bond length [C-C] (Å)	1.386	1.386	1.389
bond length [C-H] (Å)	1.079	—	1.096
bond length [C-F] (Å)	1.344	1.340	1.346
bond angle [\angle C(H)-C(F)-C(H)]	123.2°	122.97°	123.9°
bond angle [\angle C(F)-C(H)-C(F)]	116.8°	117.03°	
bond angle [\angle H-C(H)-C(F)]	121.6°	—	
bond angle [\angle F-C(F)-C(H)]	118.4°	118.51°	

^afrequencies of normal modes calculated by MP2/cc-pVDZ.¹

^bfrequencies of normal modes calculated by MP2/cc-pVTZ.¹⁰

^cdistances and angles obtained from electron diffraction studies.¹¹

TABLE S2: Fundamental Vibrational Frequencies of TFBz molecule evaluated from MP2 approach using cc-pVDZ basis set and its comparison with other theoretical findings and experimental data

Normal Mode	Optimization Result (MP2/cc-pVDZ) (cm ⁻¹) ^a	Optimization Result (MP2/cc-pVTZ) (cm ⁻¹) ^b	Experimental Result (cm ⁻¹) ^c	Nature of Vibration	Symmetry
Q_1	3259	3269	3076	symmetric C-H stretching	a'_1
Q_2	1385	1405	1363	symmetric C-F stretching	a'_1
Q_3	1026	1028	1012	trigonal distortion	a'_1
Q_4	581	584	584	ring breathing	a'_1
Q_5	1466	1467	1294	C-C stretching	a'_2
Q_6	1204	1215	1165	C-H in-plane bending	a'_2
Q_7	552	556	564	C-F in-plane bending	a'_2
Q_{8x} and Q_{8y}	3260	3271	3116	C-H asymmetric stretching	e'
Q_{9x} and Q_{9y}	1665	1676	1622	asymmetric C-C stretching	e'
Q_{10x} and Q_{10y}	1498	1509	1475	symmetric C-C stretching	e'
Q_{11x} and Q_{11y}	1136	1152	1129	C-H in-plane bending	e'
Q_{12x} and Q_{12y}	1009	1017	996	C-C-C scissoring	e'
Q_{13x} and Q_{13y}	499	502	504	C-C-C in-plane bending	e'
Q_{14x} and Q_{14y}	325	327	328	C-F scissoring	e'
Q_{15}	826	840	847	C-C twisting	a''_2
Q_{16}	628	673	663	C-C out of plane bending	a''_2
Q_{17}	206	212	207	C-F out of plane bending	a''_2
Q_{18x} and Q_{18y}	844	852	792	C-C twisting	e''
Q_{19x} and Q_{19y}	600	612	598	C-C out of plane bending	e''
Q_{20x} and Q_{20x}	247	252	246	C-F out of plane bending	e''

^afrequencies of normal modes calculated by MP2/cc-pVDZ.¹

^bfrequencies of normal modes calculated by MP2/cc-pVTZ.¹⁰

^cfrequencies of normal modes measured by IR/Raman spectroscopy.¹²

S7 Adiabatic Potential Energy Curves (PECs) and NACTs of TFBz⁺ Radical Cation

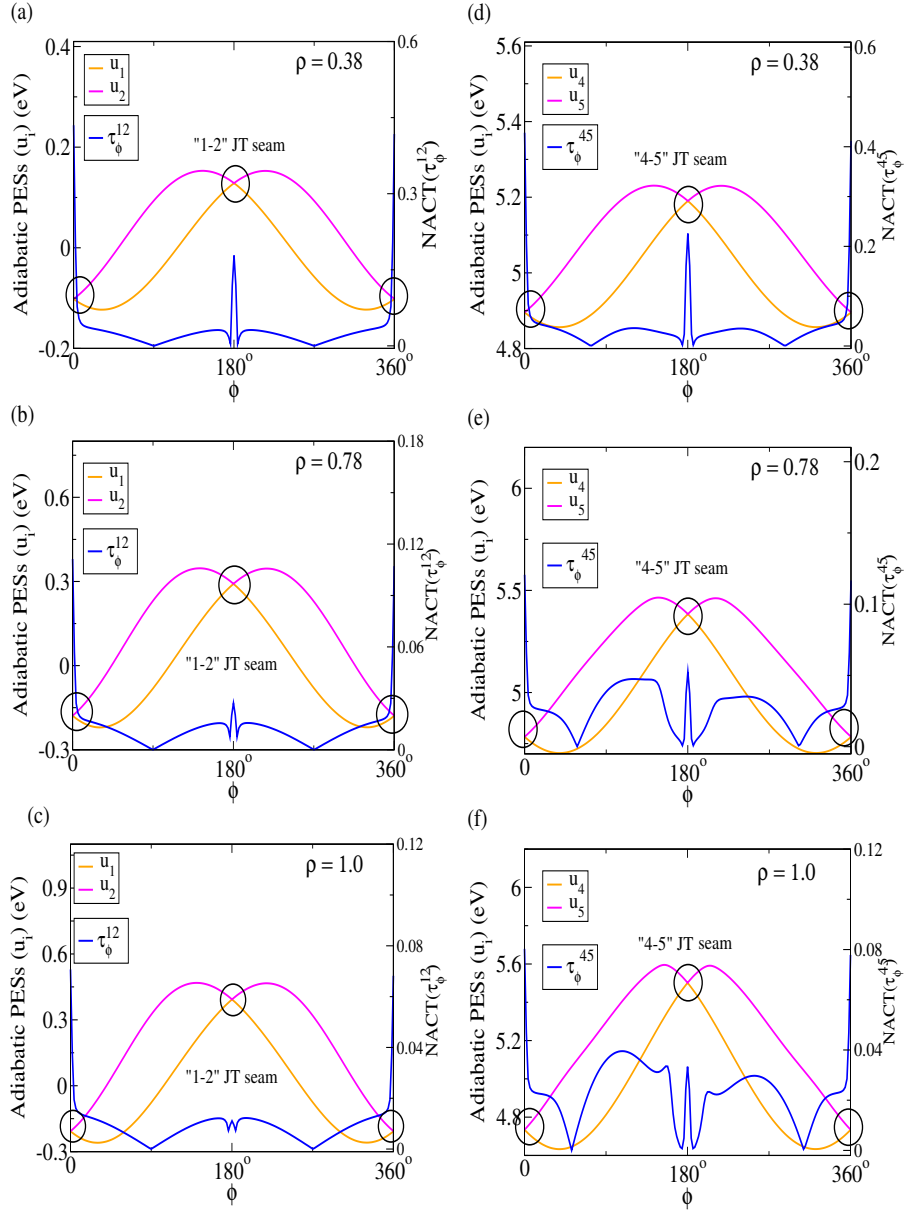


FIG. S4: The figure displays the location of “1-2” and “4-5” Jahn-Teller (JT) seams over $Q_2 - Q_{9x}$ plane: 1D cuts of adiabatic PESs are plotted for (a-c) \tilde{X}^2E'' (u_1 and u_2) and (d-f) \tilde{B}^2E' (u_4 and u_5) states along ϕ axis keeping the value of ρ at (a,d) 0.38, (b,e) 0.78 and (c,f) 1.0. The corresponding NACTs, (a-c) τ_ϕ^{12} and (d-f) τ_ϕ^{45} carry the signature of those “1-2” and “4-5” JT seams.

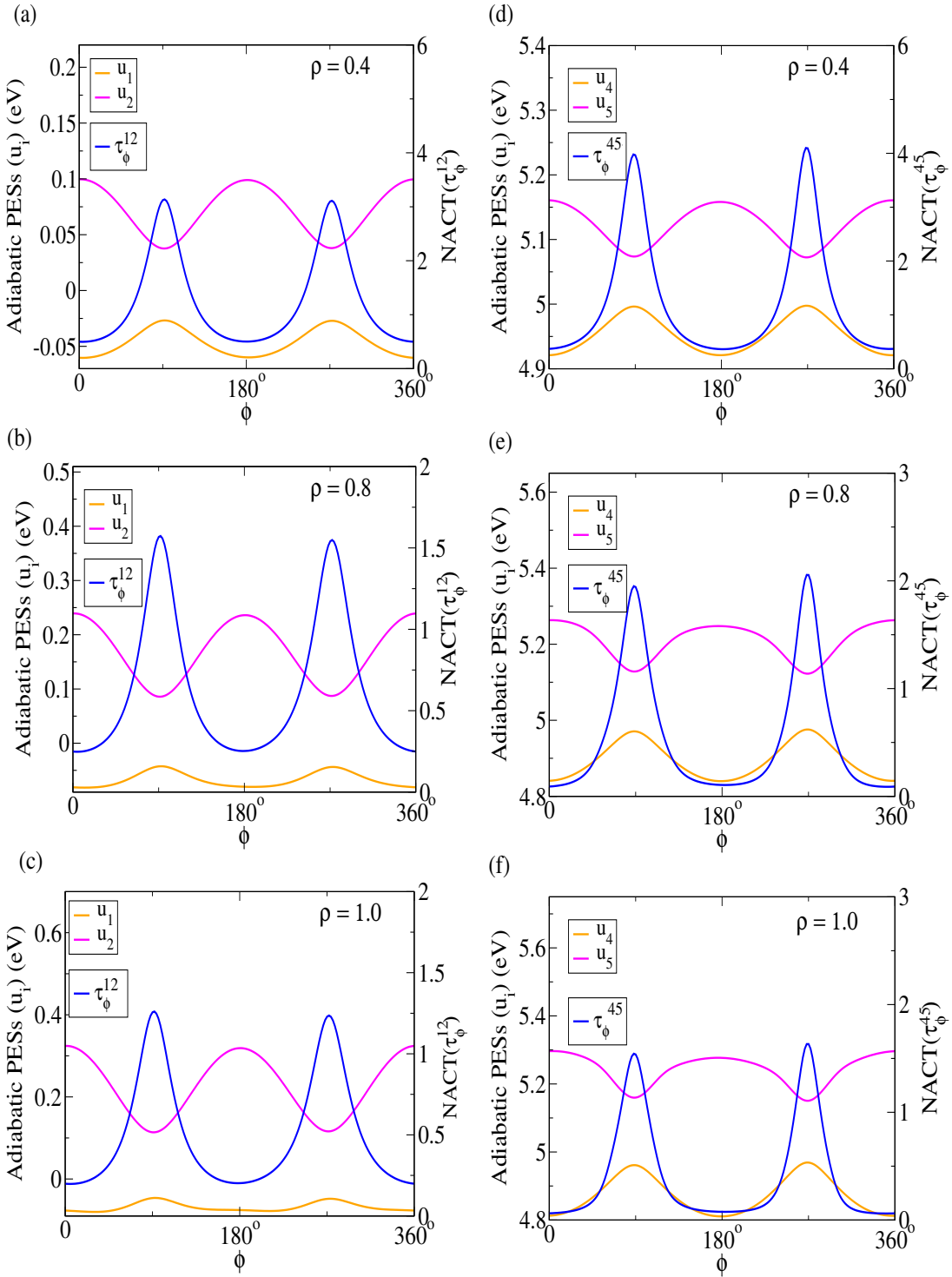


FIG. S5: For $Q_{9x} - Q_{13x}$ pair, 1D functional forms of adiabatic PESs are plotted for (a-c) \tilde{X}^2E'' (u_1 and u_2) and (d-f) \tilde{B}^2E' (u_4 and u_5) states along ϕ axis keeping the value of ρ at (a,d) 0.38, (b,e) 0.78 and (c,f) 1.0. The corresponding NACTs, (a-c) τ_ϕ^{12} and (d-f) τ_ϕ^{45} carry the signature of the “1-2” and “4-5” JT seams, which look like avoided crossings.

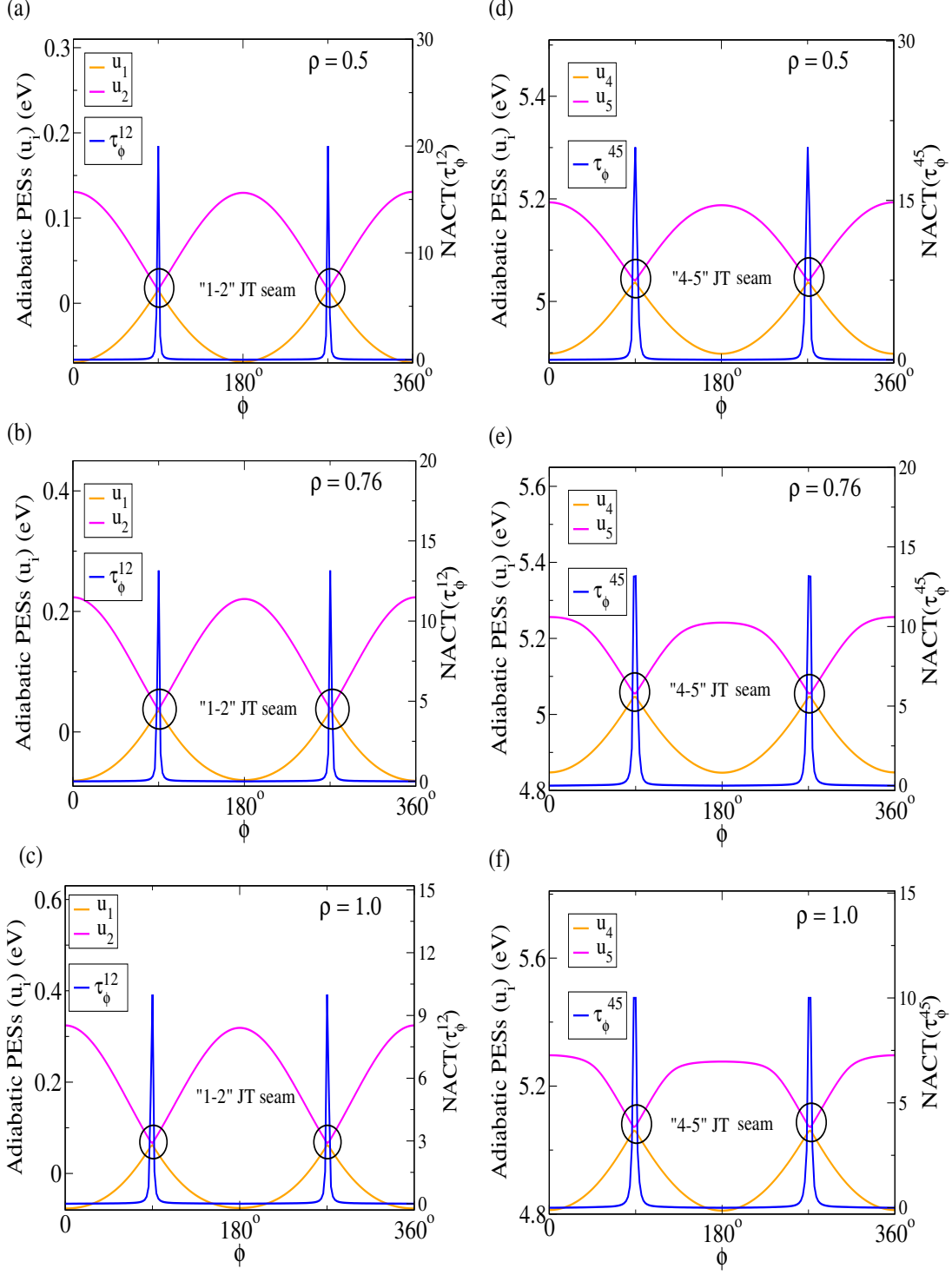


FIG. S6: In case of $Q_{9x} - Q_{18x}$ plane, 1D functional forms of adiabatic PESs are presented for (a-c) \tilde{X}^2E'' (u_1 and u_2) and (d-f) \tilde{B}^2E' (u_4 and u_5) states along ϕ axis at three values of of ρ , (a,d) 0.5, (b,e) 0.76 and (c,f) 1.0. The associated NACTs, (a-c) τ_ϕ^{12} and (d-f) τ_ϕ^{45} show the presence of “1-2” and “4-5” JT seams.

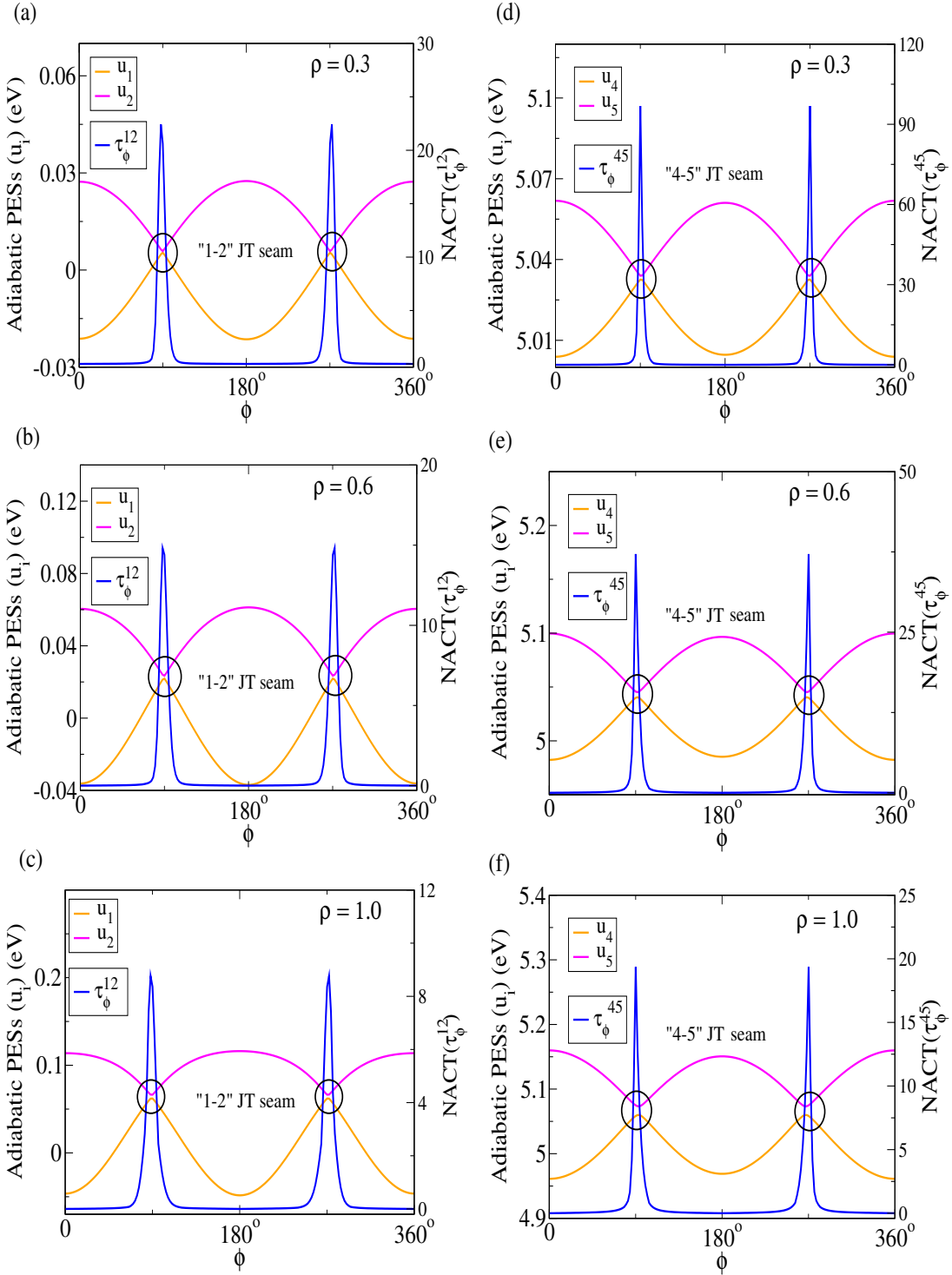


FIG. S7: The figure depicts the position of “1-2” and “4-5” JT seams over $Q_{13x} - Q_{18x}$ plane: 1D functional variation of adiabatic PESs are presented for (a-c) \tilde{X}^2E'' (u_1 and u_2) and (d-f) \tilde{B}^2E' (u_4 and u_5) states along ϕ axis at three different values of ρ (a,d) 0.3, (b,e) 0.6 and (c,f) 1.0. The associated NACTs, (a-c) τ_ϕ^{12} and (d-f) τ_ϕ^{45} show singular features at the close vicinity of the degenerate point(s).

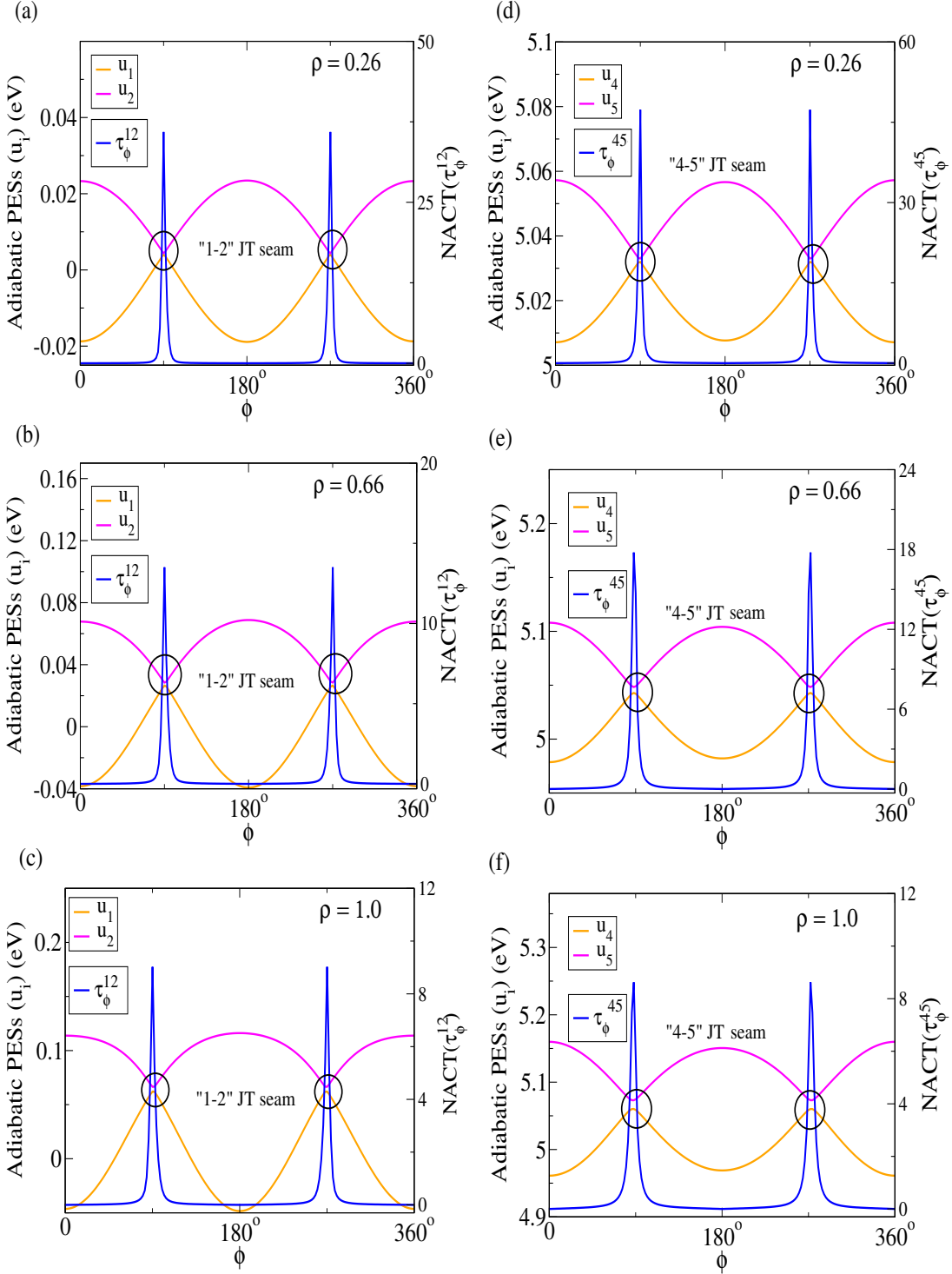


FIG. S8: For $Q_{13x} - Q_{18y}$ pair, 1D cuts of adiabatic PESs are presented for (a-c) \tilde{X}^2E'' (u_1 and u_2) and (d-f) \tilde{B}^2E' (u_4 and u_5) states along ϕ axis at three different values of ρ (a,d) 0.26, (b,e) 0.66 and (c,f) 1.0. The associated NACTs, (a-c) τ_ϕ^{12} and (d-f) τ_ϕ^{45} show singular features at the close vicinity of “1-2” and “4-5” JT seams.

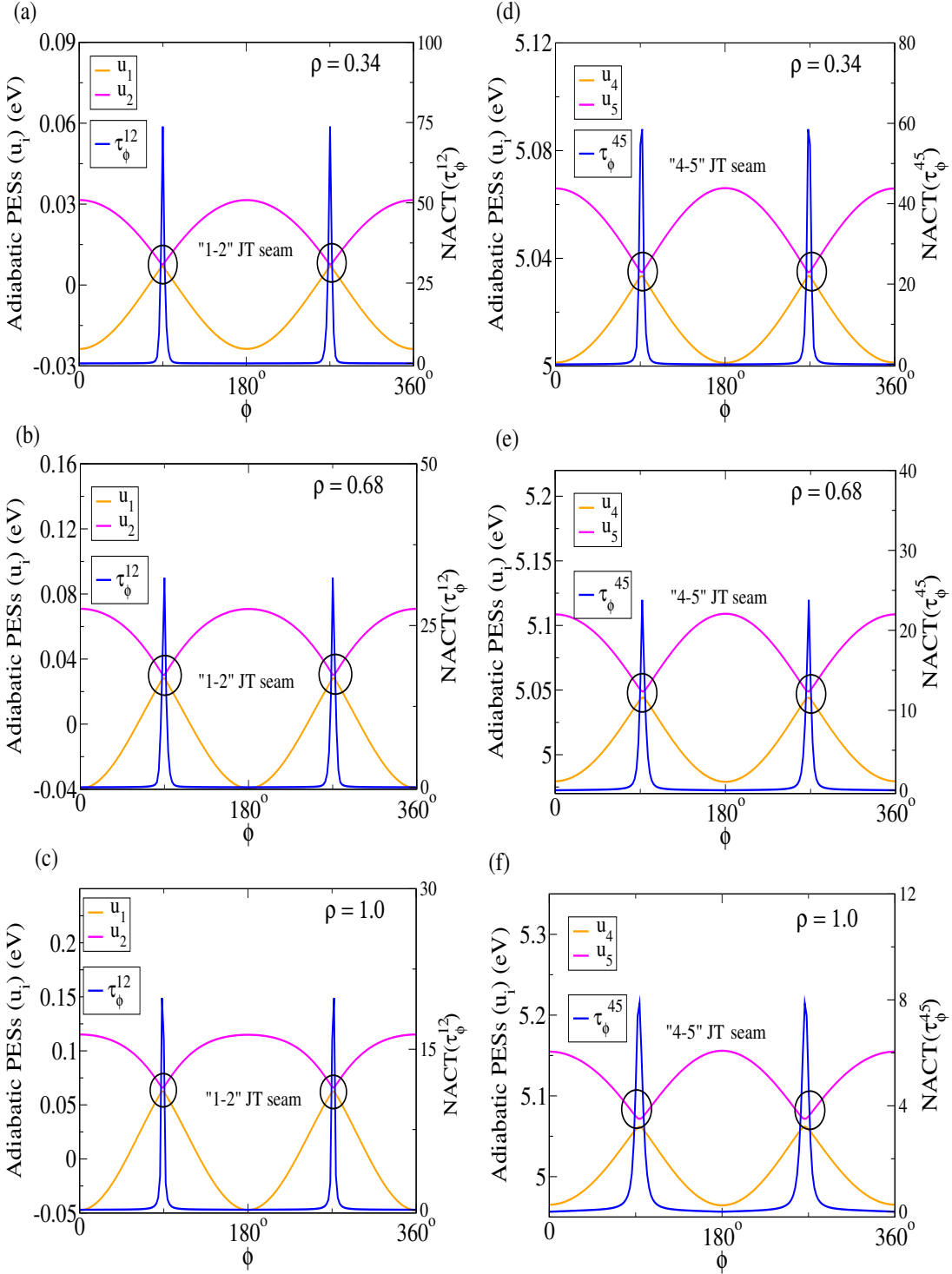


FIG. S9: In case of $Q_{13y} - Q_{18x}$ pair, 1D functional forms of adiabatic PESs are presented for (a-c) \tilde{X}^2E'' (u_1 and u_2) and (d-f) \tilde{B}^2E' (u_4 and u_5) states along ϕ axis at three fixed values of ρ (a,d) 0.34, (b,e) 0.68 and (c,f) 1.0. The corresponding 1D cuts of NACTs, (a-c) τ_ϕ^{12} and (d-f) τ_ϕ^{45} tend to be singular at the close neighbourhood of “1-2” and “4-5” JT seams.

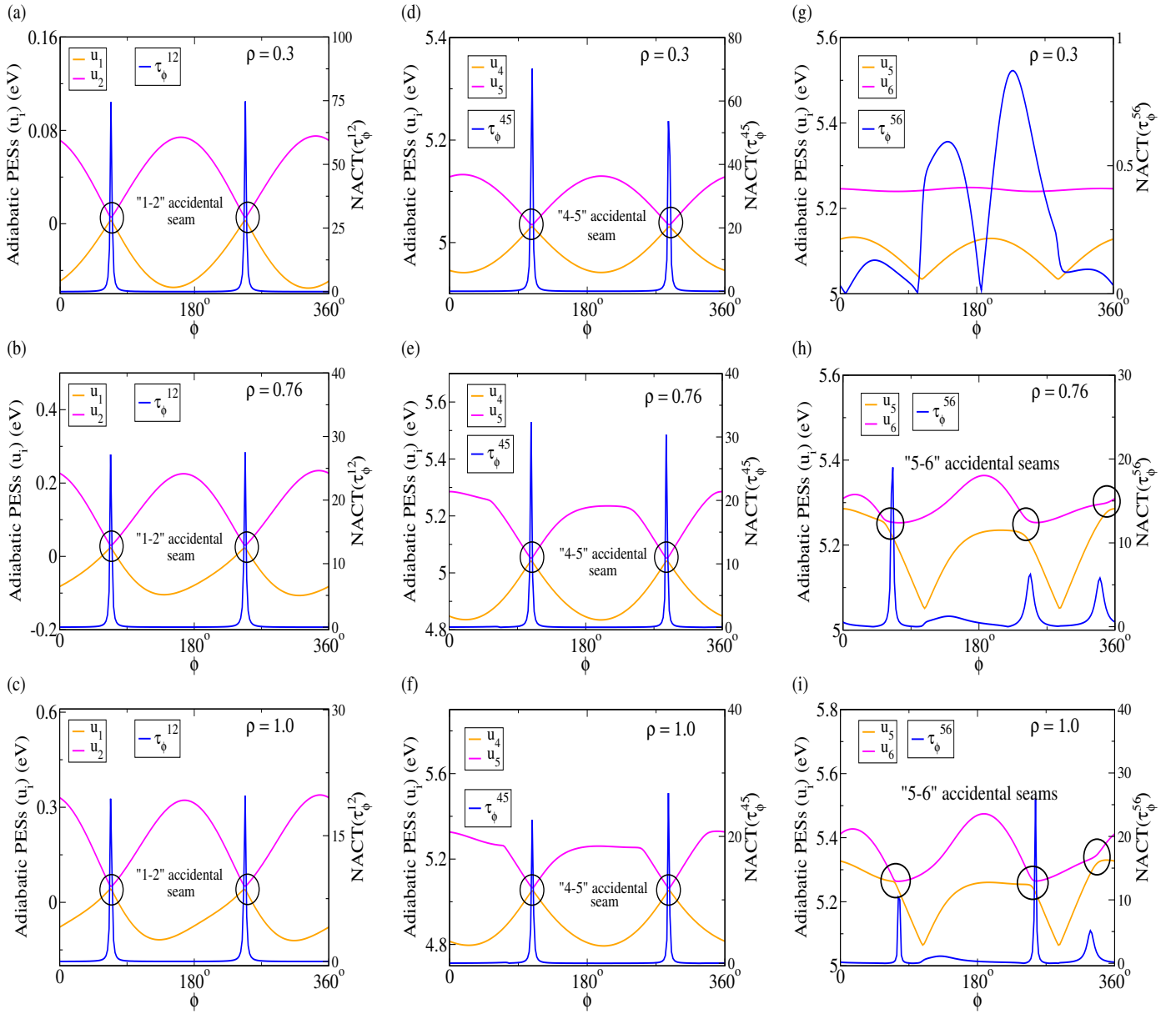


FIG. S10: The figure depicts 1D functional form of adiabatic PESs for (a-c) \tilde{X}^2E'' (u_1 and u_2), (d-f) \tilde{B}^2E' (u_4 and u_5) and (g-h) upper sheet of \tilde{B}^2E' and $\tilde{C}^2A'_2$ (u_5 and u_6) states along ϕ axis at three different values of ρ (a,d,g) 0.3, (b,e,h) 0.76 and (c,f,i) 1.0 for $Q_{9y} - Q_{13x}$ plane. The associated NACTs, (a-c) τ_ϕ^{12} , (d-f) τ_ϕ^{45} and (g-h) τ_ϕ^{56} show singular characteristics due to one “1-2”, one “4-5” and two “5-6” accidental seams.

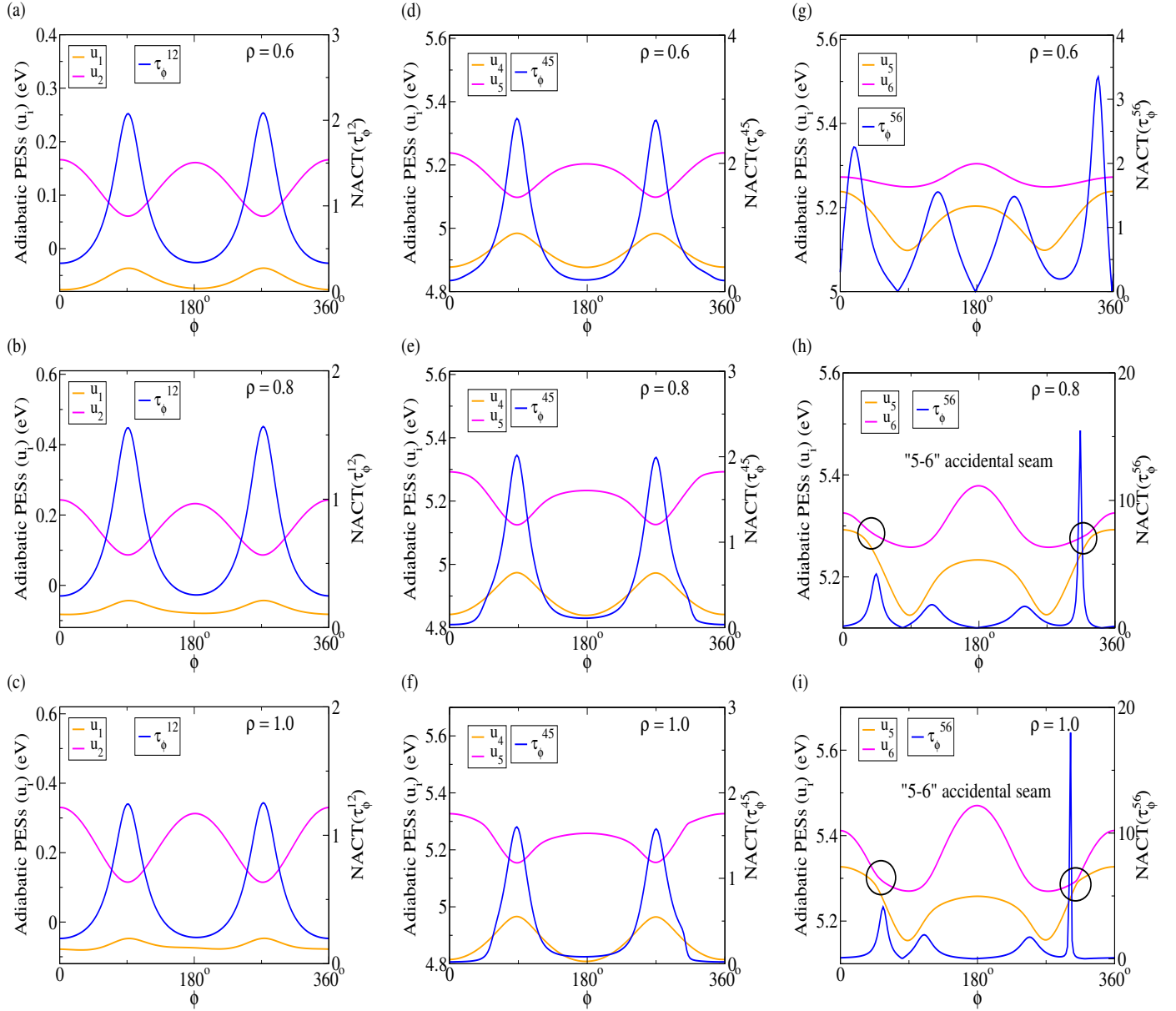


FIG. S11: The figure presents 1D cuts of adiabatic PESs for (a-c) \tilde{X}^2E'' (u_1 and u_2), (d-f) \tilde{B}^2E' (u_4 and u_5) and (g-h) upper sheet of \tilde{B}^2E' and $\tilde{C}^2A'_2$ (u_5 and u_6) states along ϕ axis at three fixed values of ρ (a,d,g) 0.6, (b,e,h) 0.8 and (c,f,i) 1.0 for $Q_{9y} - Q_{13y}$ pair. The relevant NACTs, (a-c) τ_ϕ^{12} , (d-f) τ_ϕ^{45} and (g-h) τ_ϕ^{56} steeply rise at and around the “1-2” JT seam, “4-5” JT seam and “5-6” accidental seam. The seams look like avoided crossings.

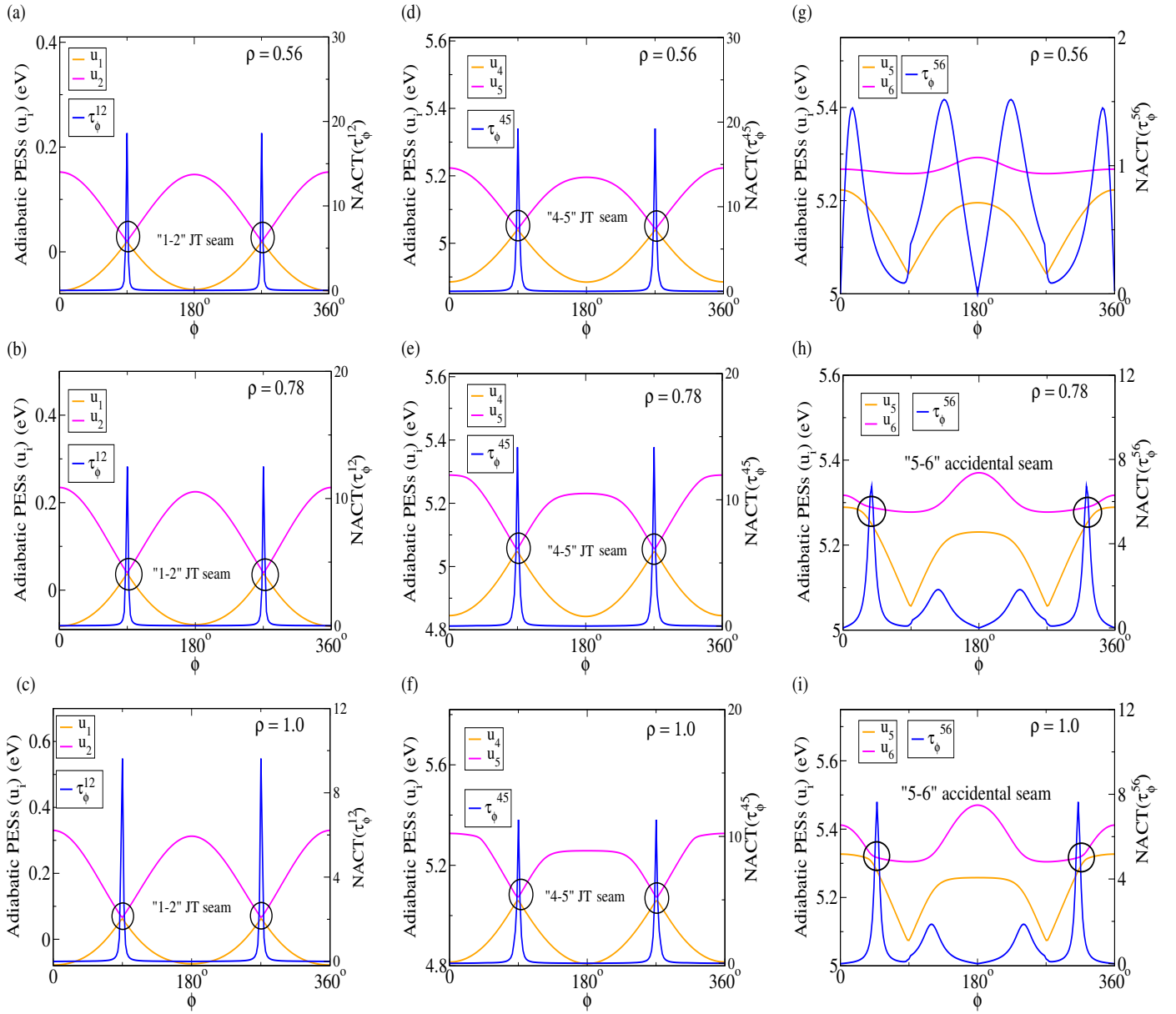


FIG. S12: In case of $Q_{9y} - Q_{18y}$ pair, 1D functional forms of adiabatic PESs for (a-c) \tilde{X}^2E'' (u_1 and u_2), (d-f) \tilde{B}^2E' (u_4 and u_5) and (g-h) upper sheet of \tilde{B}^2E' and $\tilde{C}^2A'_2$ (u_5 and u_6) states are plotted along ϕ axis at three different values of ρ (a,d,g) 0.56, (b,e,h) 0.78 and (c,f,i) 1.0. The associated NACTs, (a-c) τ_ϕ^{12} , (d-f) τ_ϕ^{45} and (g-h) τ_ϕ^{56} show singular features at and around the "1-2" JT seam, "4-5" JT seam and "5-6" accidental seam.

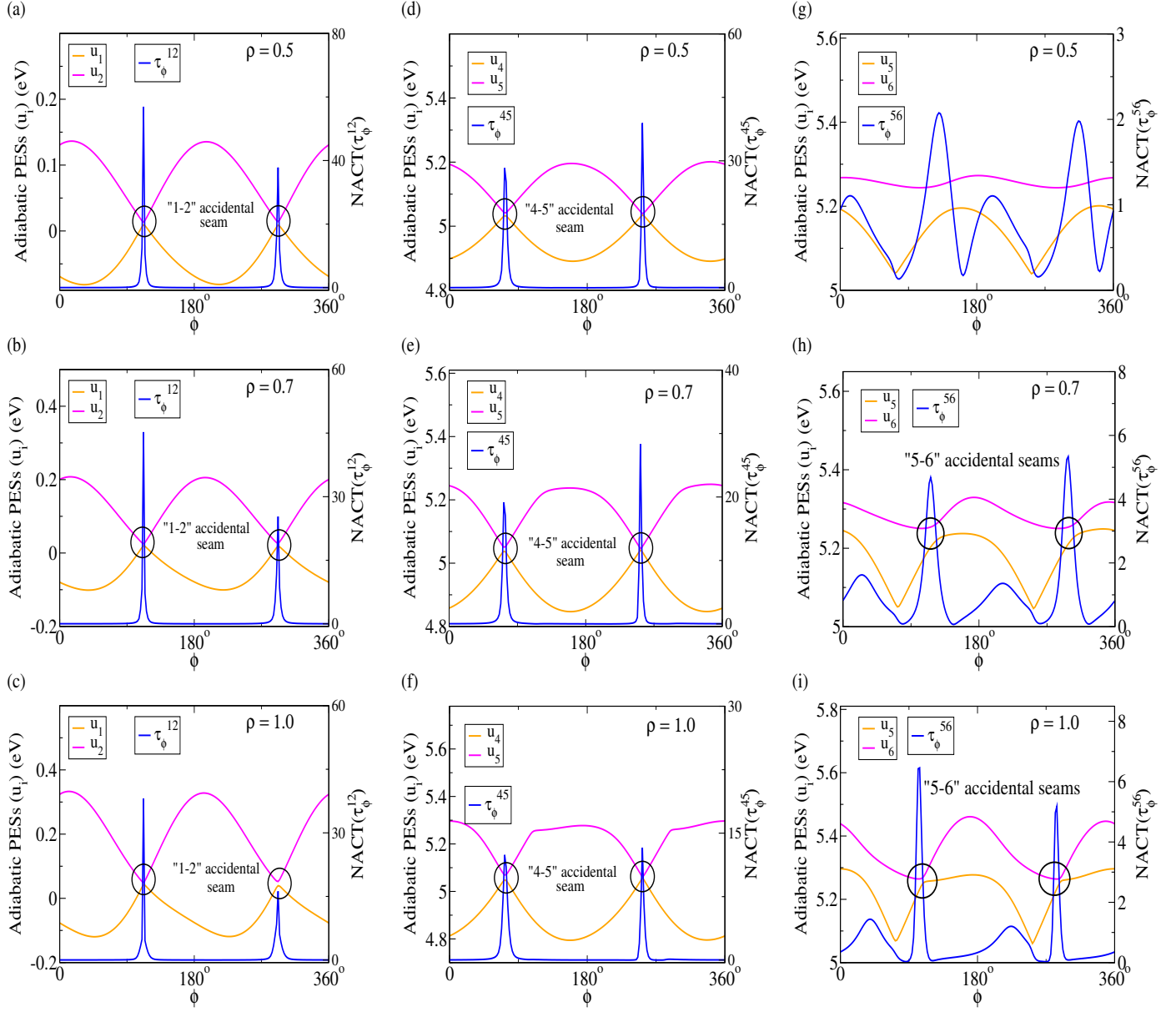


FIG. S13: The figure presents 1D cuts of adiabatic PESs for (a-c) \tilde{X}^2E'' (u_1 and u_2), (d-f) \tilde{B}^2E' (u_4 and u_5) and (g-h) upper sheet of \tilde{B}^2E' and $\tilde{C}^2A'_2$ (u_5 and u_6) states along ϕ axis keeping the value of ρ fixed at (a,d,g) 0.5, (b,e,h) 0.7 and (c,f,i) 1.0 for $Q_{9x} - Q_{13y}$ pair. The associated NACTs, (a-c) τ_ϕ^{12} , (d-f) τ_ϕ^{45} and (g-h) τ_ϕ^{56} exhibit a steep rise due to one “1-2”, one “4-5” and two “5-6” accidental seams.

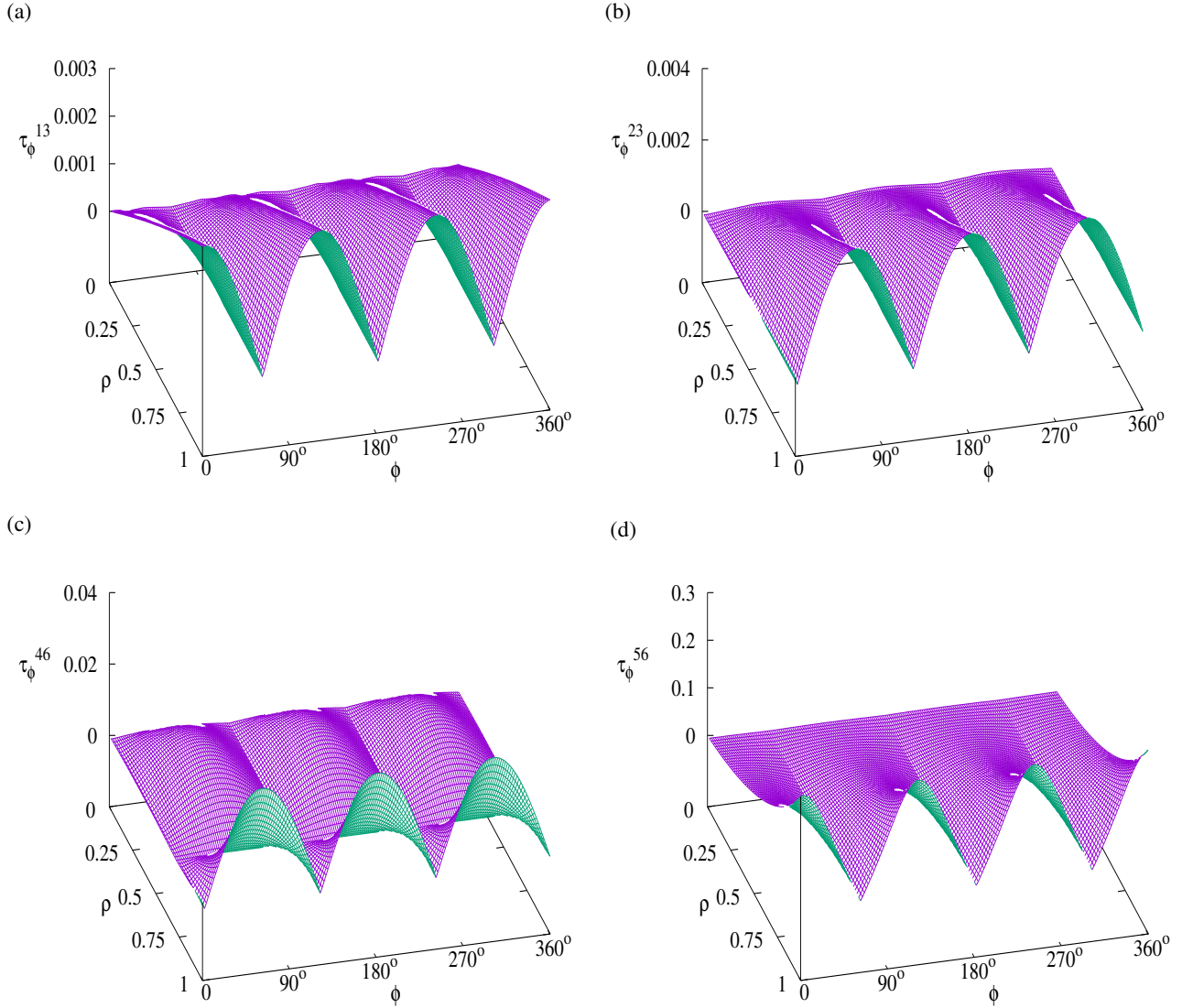


FIG. S14: The ϕ components of NACTs corresponding to (a) “1-3” (τ_{ϕ}^{13}), (b) “2-3” (τ_{ϕ}^{23}), (c) “4-6” (τ_{ϕ}^{46}) and (d) “5-6” (τ_{ϕ}^{56}) Pseudo Jahn-Teller (PJT) interactions are depicted over the polar ($\rho - \phi$) plane of $Q_{13x} - Q_{13y}$, which are non-zero in the interested domain of nuclear CS.

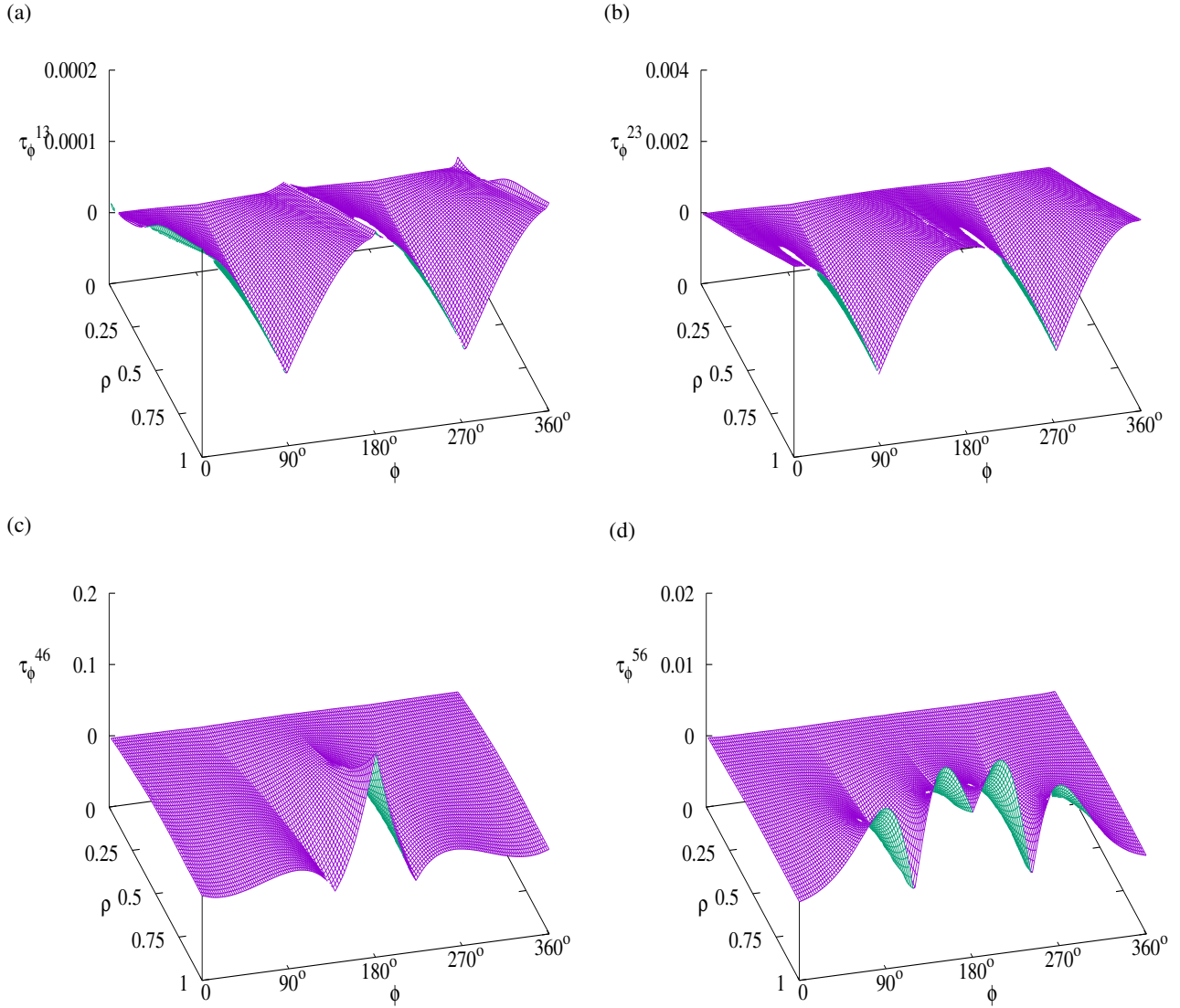


FIG. S15: The ϕ component of NACTs for $Q_2 - Q_{13x}$ plane originating from (a) “1-3” (τ_ϕ^{13}), (b) “2-3” (τ_ϕ^{23}), (c) “4-6” (τ_ϕ^{46}) and (d) “5-6” (τ_ϕ^{56}) PJT couplings are displayed for $Q_2 - Q_{13x}$ nuclear CS.

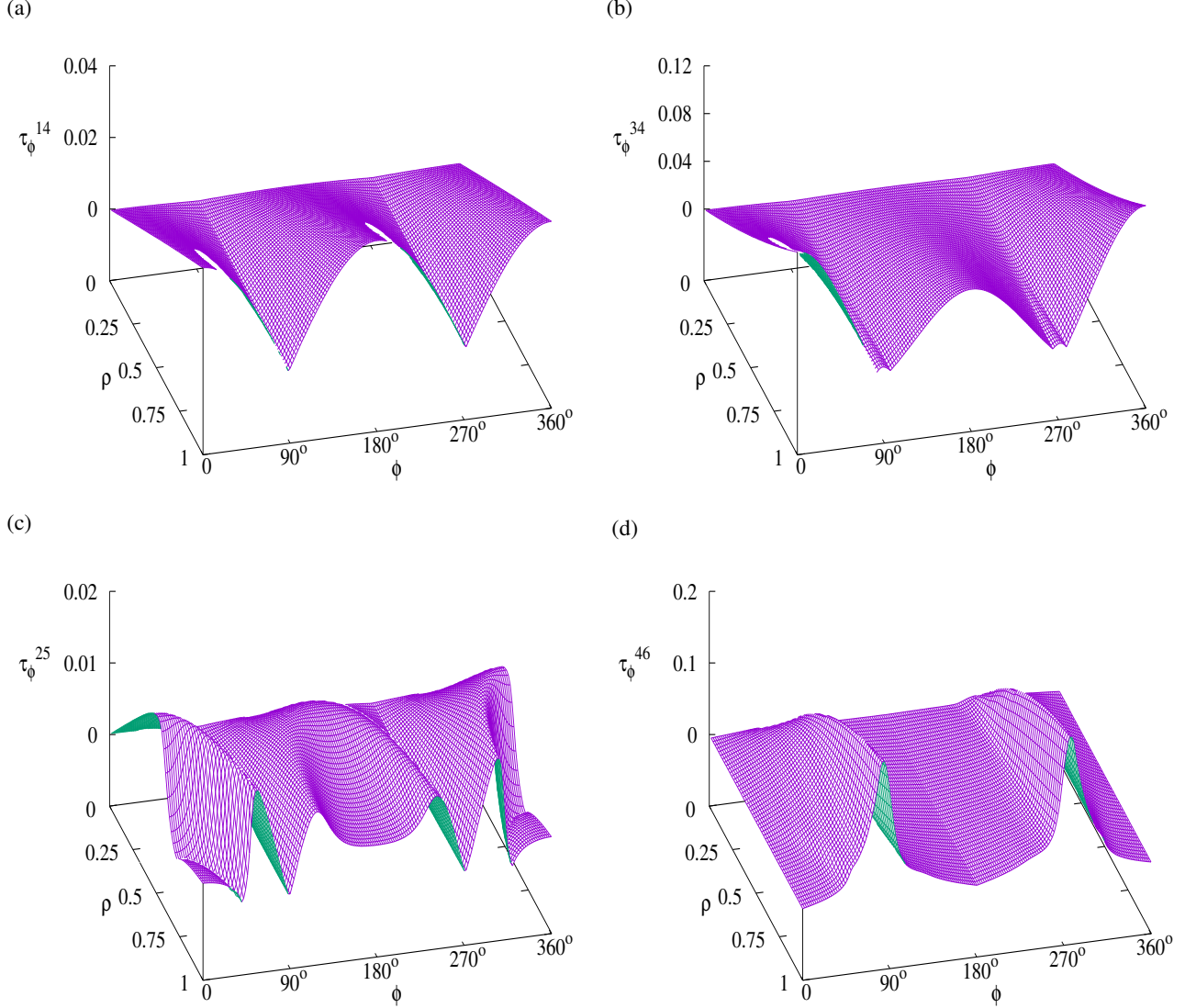


FIG. S16: The ϕ component of NACTs appearing due to (a) “1-4” (τ_ϕ^{14}), (b) “3-4” (τ_ϕ^{34}), (c) “2-5” (τ_ϕ^{25}) and (d) “4-6” (τ_ϕ^{46}) PJT couplings are depicted for $Q_{9y} - Q_{18x}$ plane.

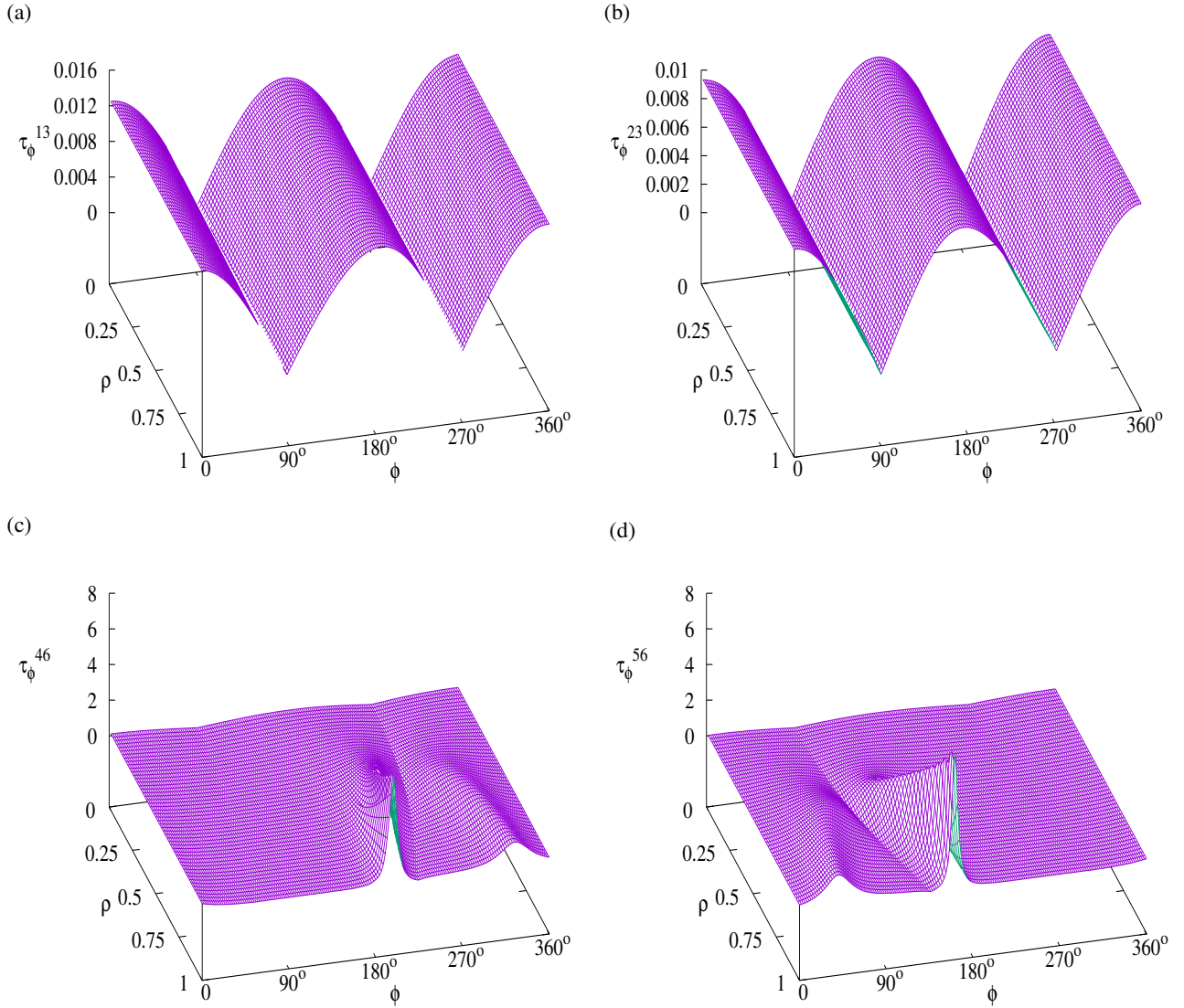


FIG. S17: The ϕ component of NACTs appearing due to (a) “1-3” (τ_ϕ^{13}), (b) “2-3” (τ_ϕ^{23}), (c) “4-6” (τ_ϕ^{46}) and (d) “5-6” (τ_ϕ^{56}) PJT couplings are displayed for $Q_2 - Q_{9x}$ nuclear CS.

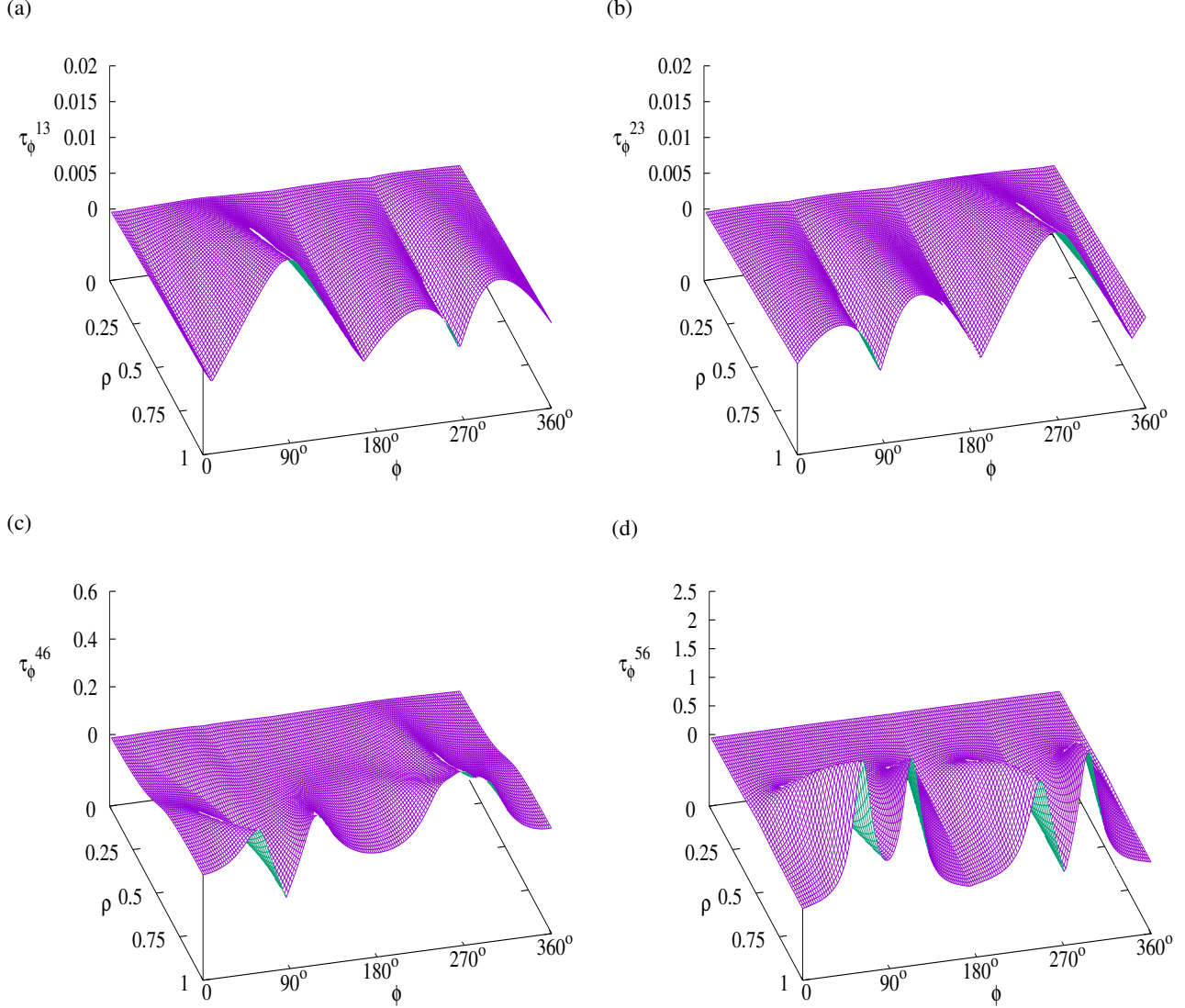


FIG. S18: The ϕ component of NACTs originated from (a) “1-3” (τ_ϕ^{13}), (b) “2-3” (τ_ϕ^{23}), (c) “4-6” (τ_ϕ^{46}) and (d) “5-6” (τ_ϕ^{56}) PJT interactions are plotted for $Q_{9x} - Q_{13x}$ nuclear CS.

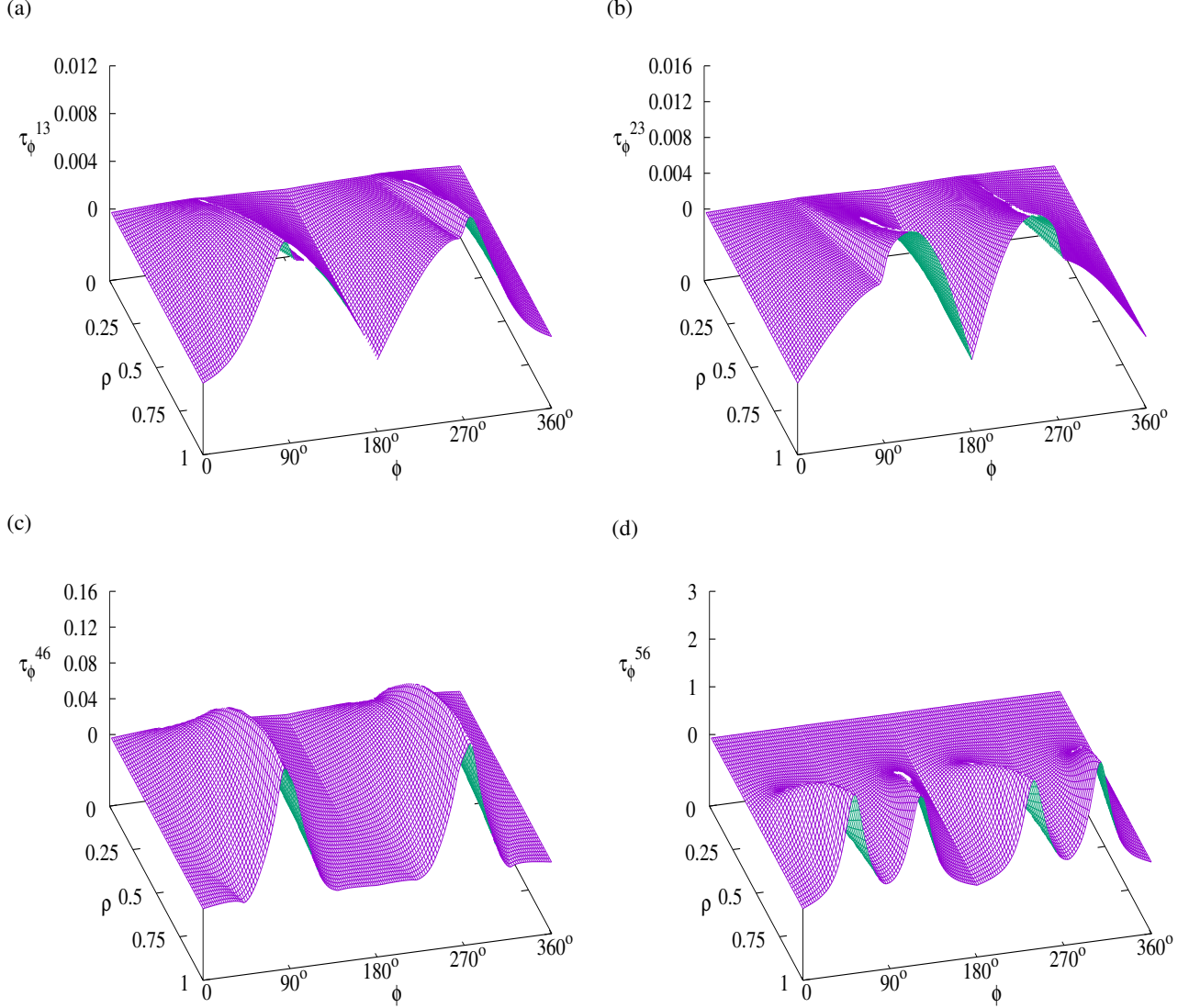


FIG. S19: The ϕ component of NACTs associated with (a) “1-3” (τ_ϕ^{13}), (b) “2-3” (τ_ϕ^{23}), (c) “4-6” (τ_ϕ^{46}) and (d) “5-6” (τ_ϕ^{56}) PJT couplings are presented for $Q_{9x} - Q_{18x}$ pair.

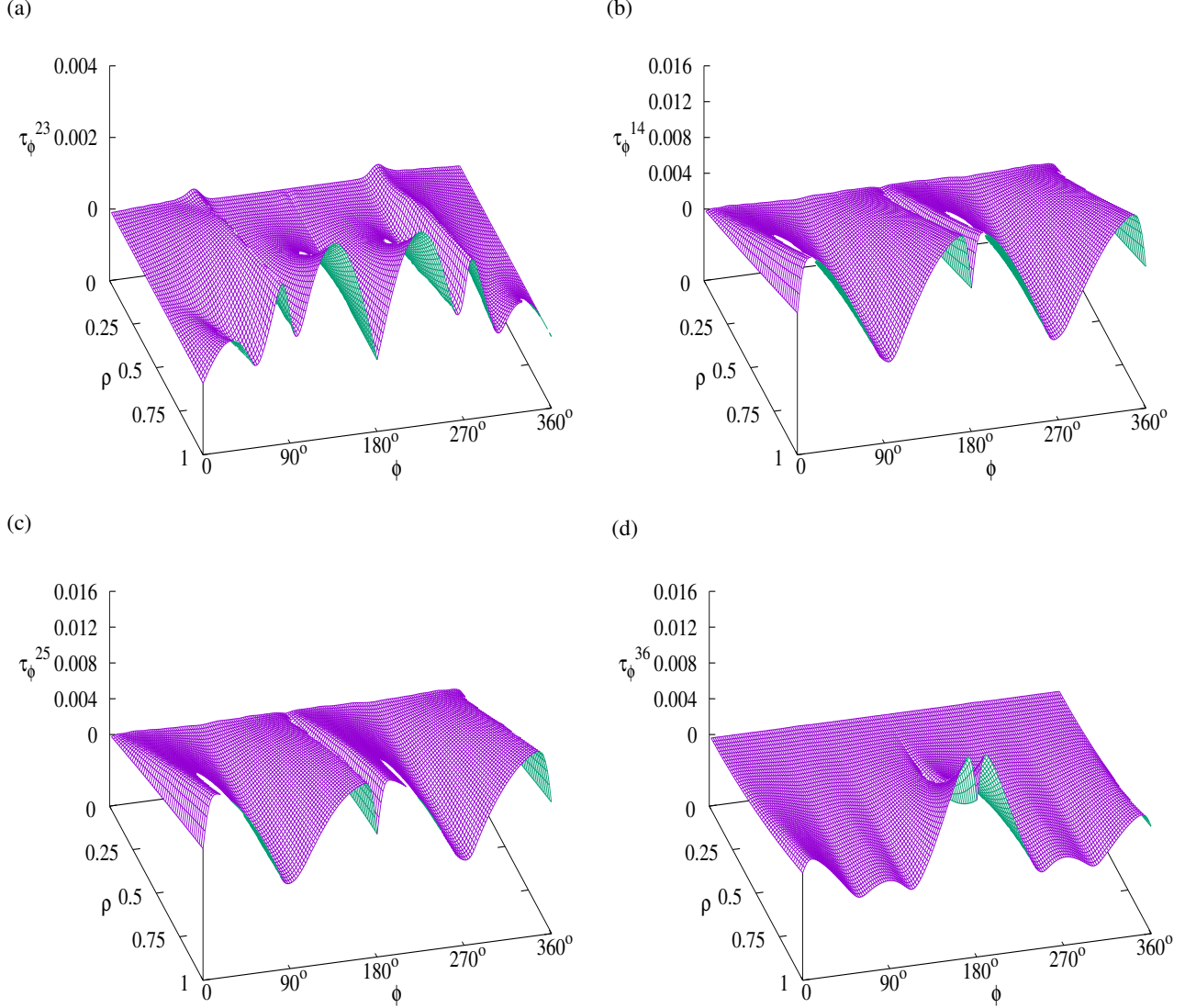


FIG. S20: The ϕ component of NACTs associated with (a) “2-3” (τ_{ϕ}^{23}), (b) “1-4” (τ_{ϕ}^{14}), (c) “2-5” (τ_{ϕ}^{25}) and (d) “4-6” (τ_{ϕ}^{46}) PJT couplings are depicted for $Q_{13x} - Q_{18x}$ nuclear plane.

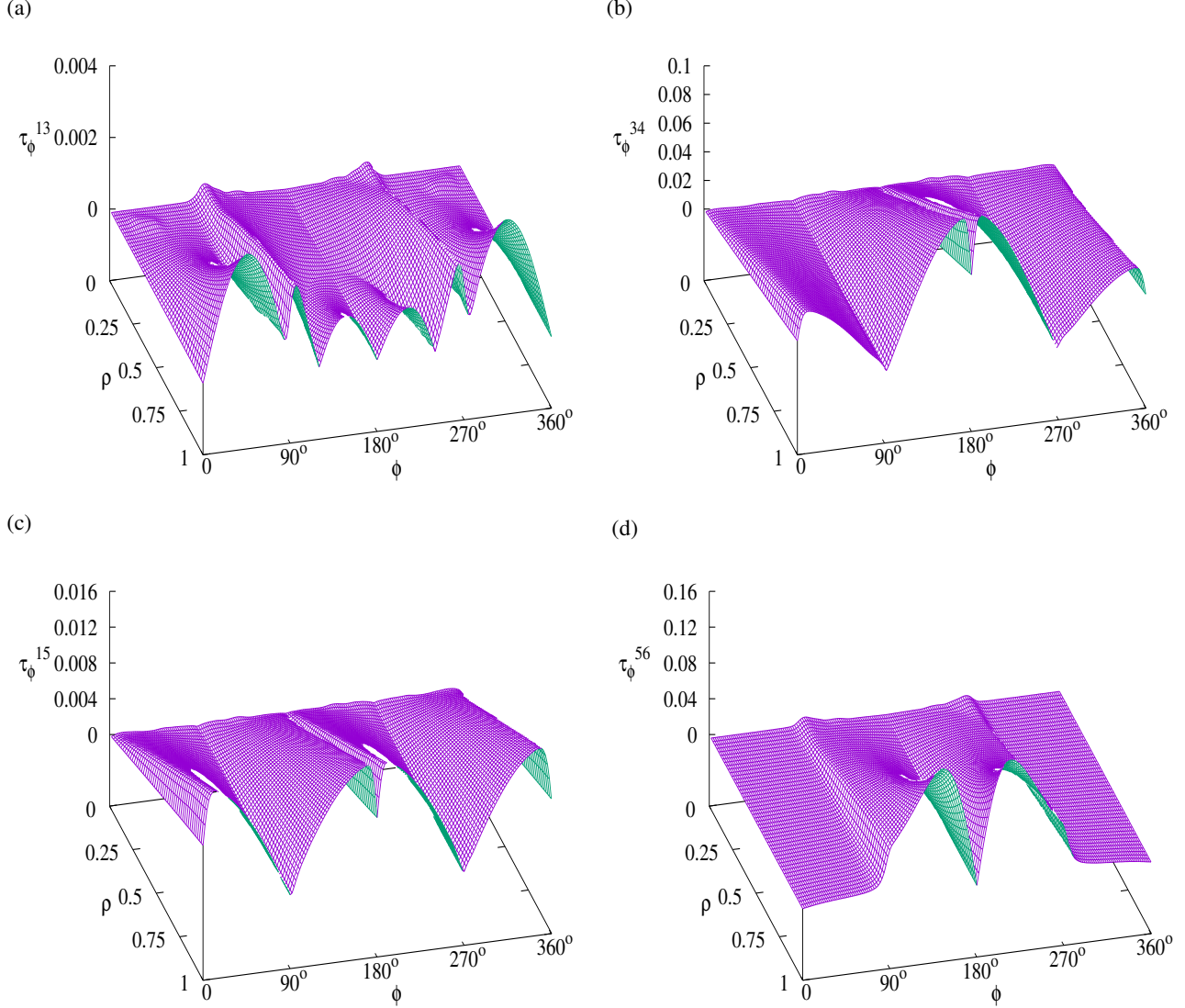


FIG. S21: The ϕ component of NACTs representing (a) “1-3” (τ_ϕ^{13}), (b) “3-4” (τ_ϕ^{34}), (c) “1-5” (τ_ϕ^{15}) and (d) “5-6” (τ_ϕ^{56}) PJT interactions are presented for $Q_{13x} - Q_{18y}$ nuclear plane.

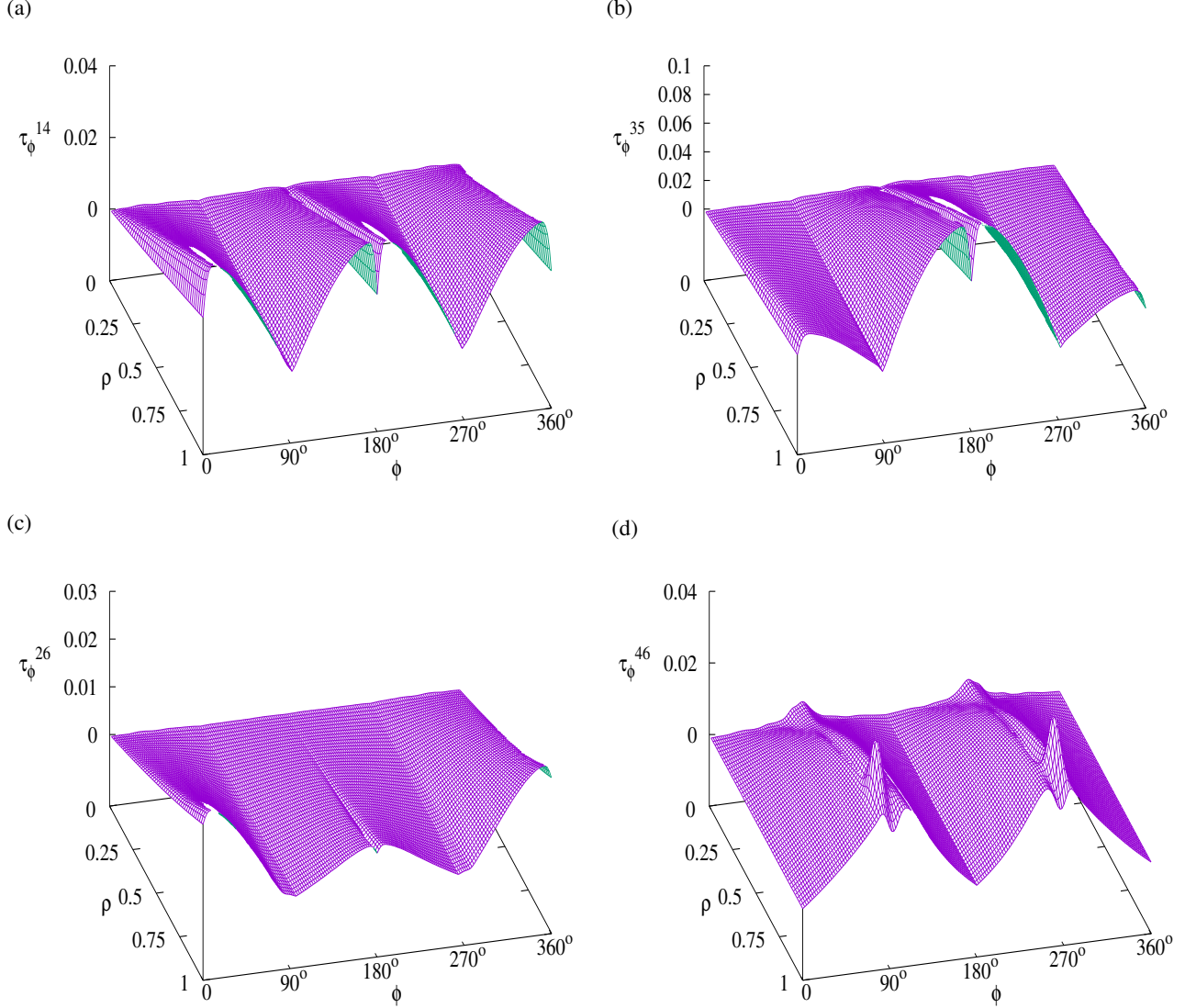


FIG. S22: The ϕ component of NACTs originating from (a) “1-4” (τ_ϕ^{14}), (b) “3-5” (τ_ϕ^{35}), (c) “2-6” (τ_ϕ^{26}) and (d) “4-6” (τ_ϕ^{46}) PJT interactions are presented for $Q_{13y} - Q_{18x}$ nuclear plane.

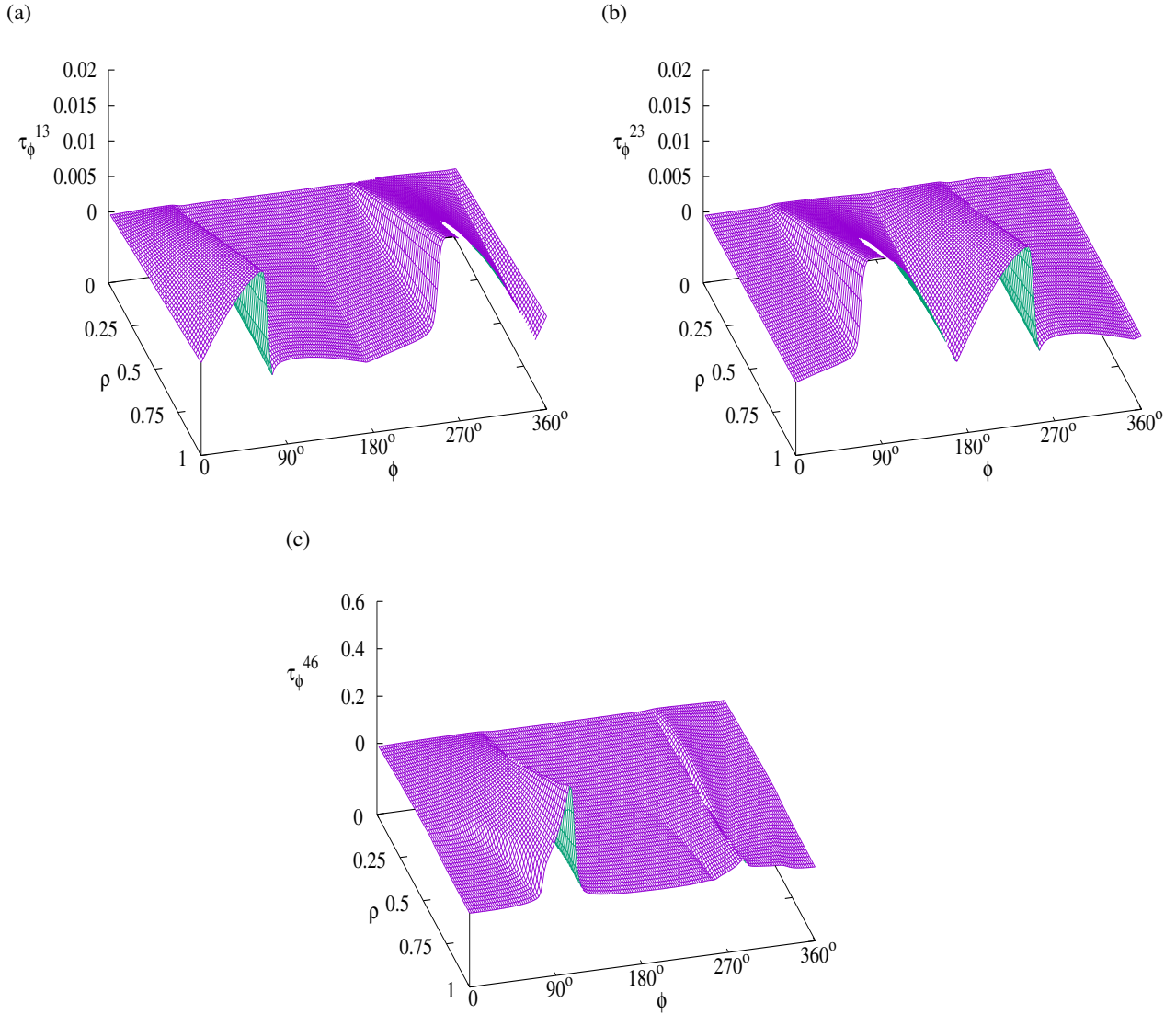


FIG. S23: For $Q_{9y} - Q_{13x}$ nuclear plane, the ϕ component of NACTs corresponding to (a) “1-3” (τ_{ϕ}^{13}), (b) “2-3” (τ_{ϕ}^{23}) and (c) “4-6” (τ_{ϕ}^{46}) PJT interactions are displayed over $\rho - \phi$ plane.

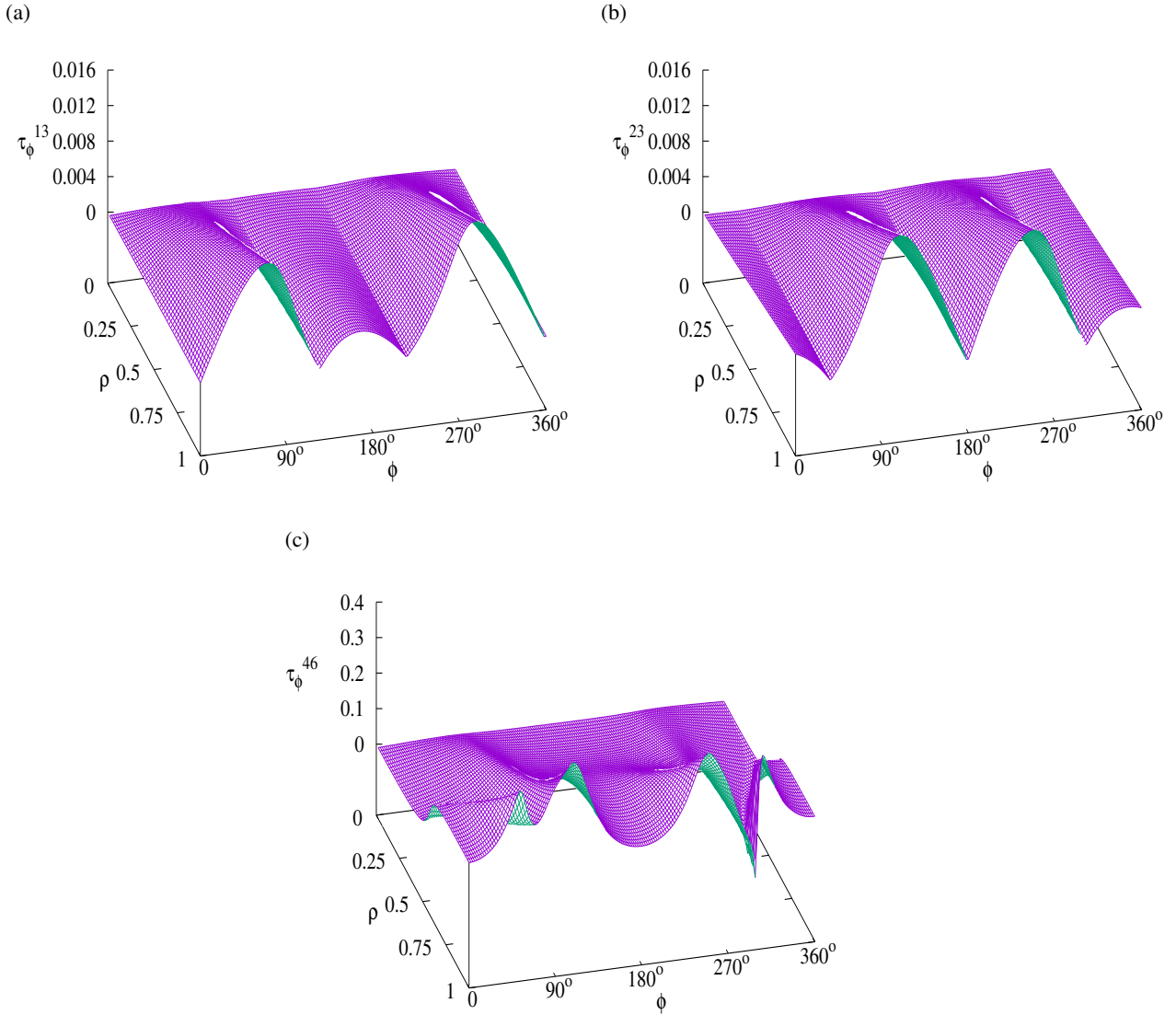


FIG. S24: In case of $Q_{9y} - Q_{13y}$ nuclear CS, the ϕ component of NACTs associated with (a) “1-3” (τ_ϕ^{13}), (b) “2-3” (τ_ϕ^{23}) and (c) “4-6” (τ_ϕ^{46}) PJT couplings are plotted over $\rho - \phi$ plane.

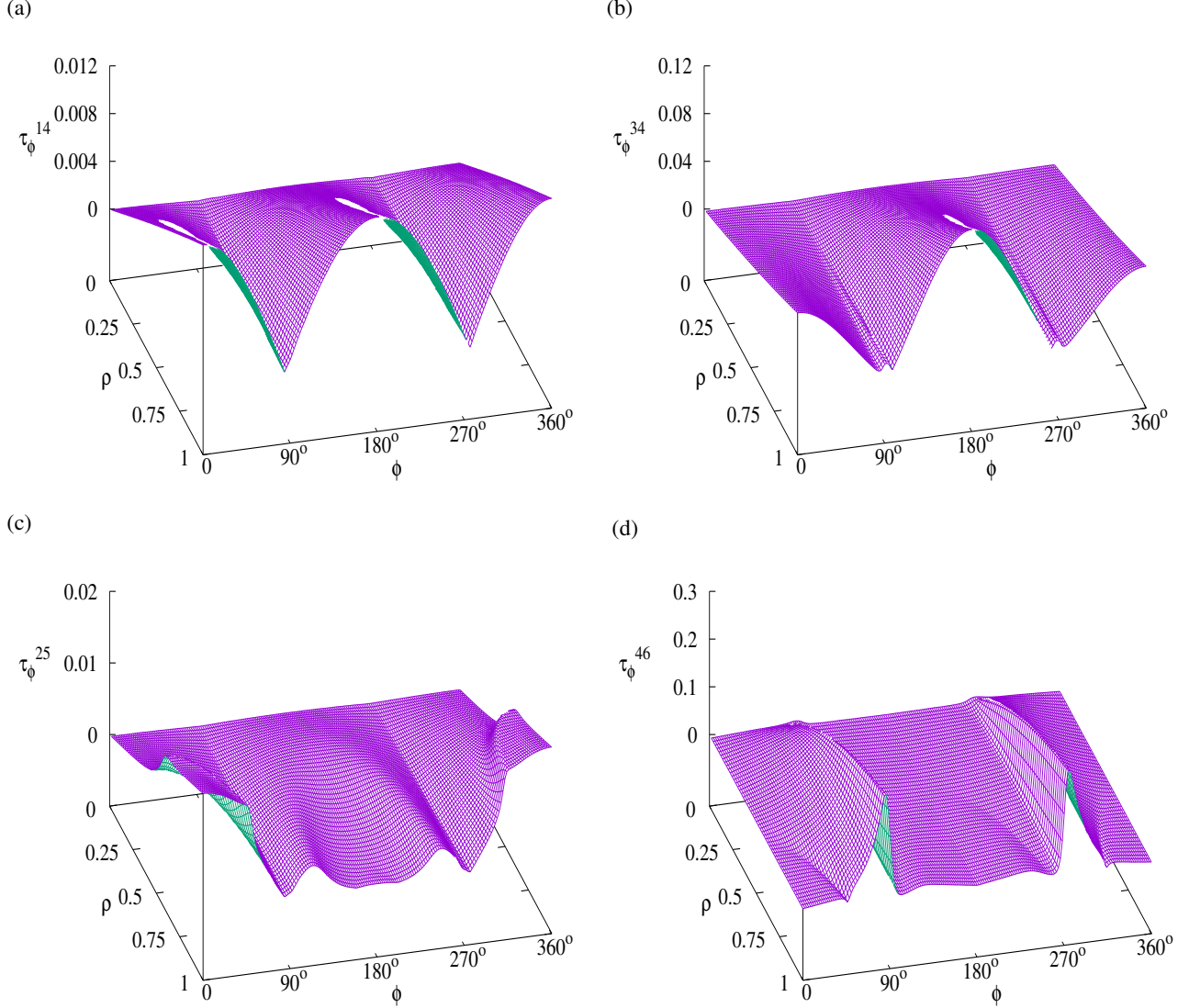


FIG. S25: In case of $Q_{9y} - Q_{18y}$ nuclear CS, the ϕ component of NACTs representing (a) “1-4” (τ_ϕ^{14}), (b) “3-4” (τ_ϕ^{34}), (c) “2-5” (τ_ϕ^{25}) and (d) “4-6” (τ_ϕ^{46}) PJT couplings are depicted over the polar plane, $\rho - \phi$.

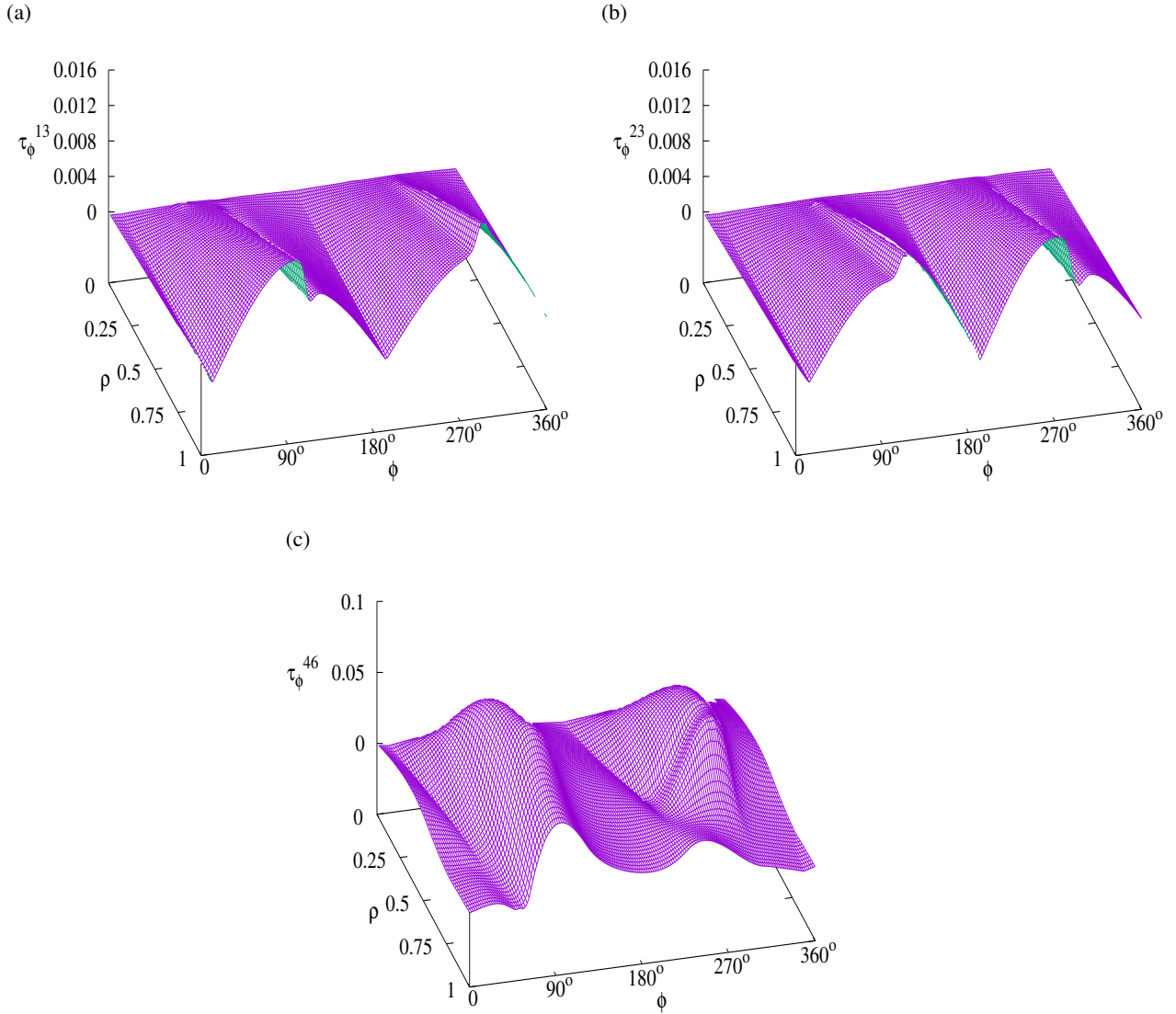


FIG. S26: For $Q_{9x} - Q_{13y}$ pairwise normal modes, the ϕ component of NACTs representing (a) “1-3” (τ_{ϕ}^{13}), (b) “2-3” (τ_{ϕ}^{23}) and (c) “4-6” (τ_{ϕ}^{46}) PJT couplings are depicted over $\rho - \phi$ plane.

S8 ADT Angles, Diagonal Elements of ADT Matrices and Diabatic PESs of TFBz⁺ Radical Cation

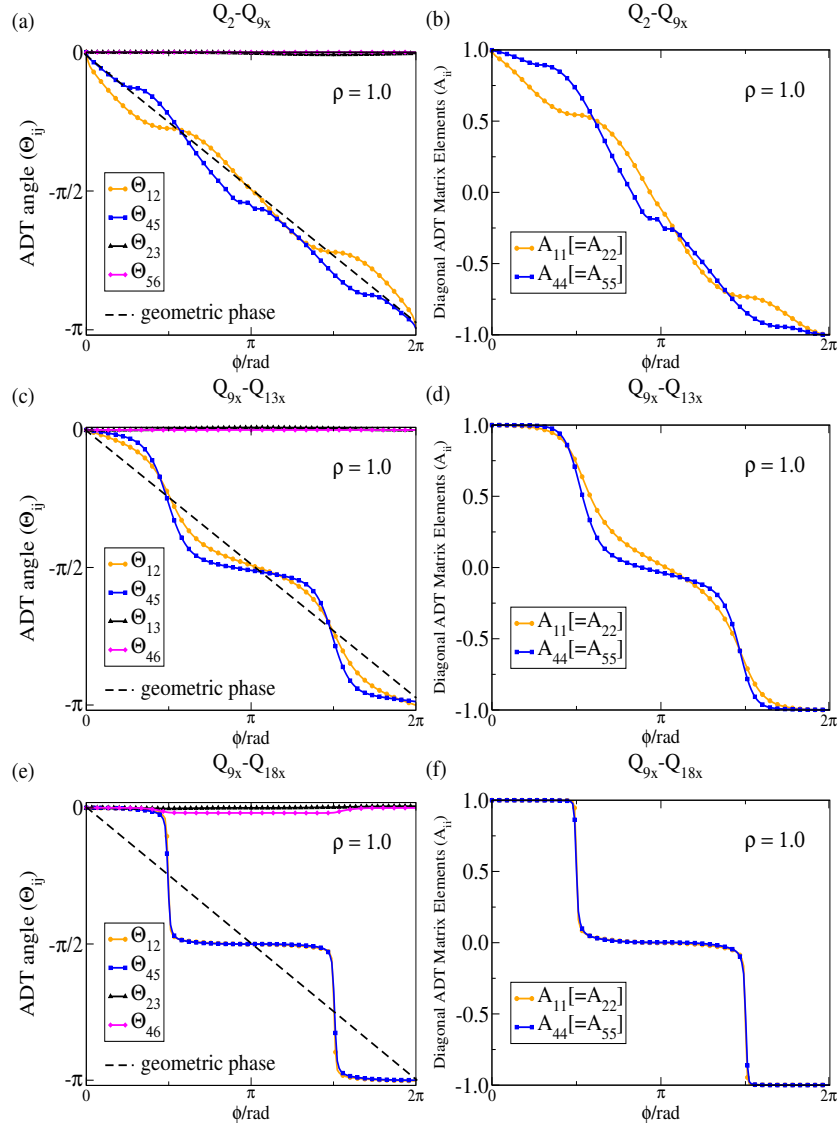


FIG. S27: The left column shows 1D functional forms of ADT angles, namely, (a) Θ_{12} , Θ_{45} , Θ_{23} and Θ_{56} for $Q_2 - Q_{9x}$ pair; (c) Θ_{12} , Θ_{45} , Θ_{13} and Θ_{46} for $Q_{9x} - Q_{13x}$ pair and (e) Θ_{12} , Θ_{45} , Θ_{26} and Θ_{56} for $Q_{9x} - Q_{18x}$ pair along ϕ coordinate at a fixed value of ρ ($= 1.0$). The right column presents 1D cuts of diagonal elements of ADT matrices, viz., $A_{11} [= A_{22}]$ and $A_{44} [= A_{55}]$ for (b) $Q_2 - Q_{9x}$, (d) $Q_{9x} - Q_{13x}$ and (f) $Q_{9x} - Q_{18x}$ pairs along the ϕ coordinate at the same value of ρ . The ADT angles associated with “1-2” and “4-5” JT/accidental seams acquire the magnitude of π at the end of the contour ($\phi = 2\pi$) and the diagonal elements of the ADT matrices undergo one sign inversion.

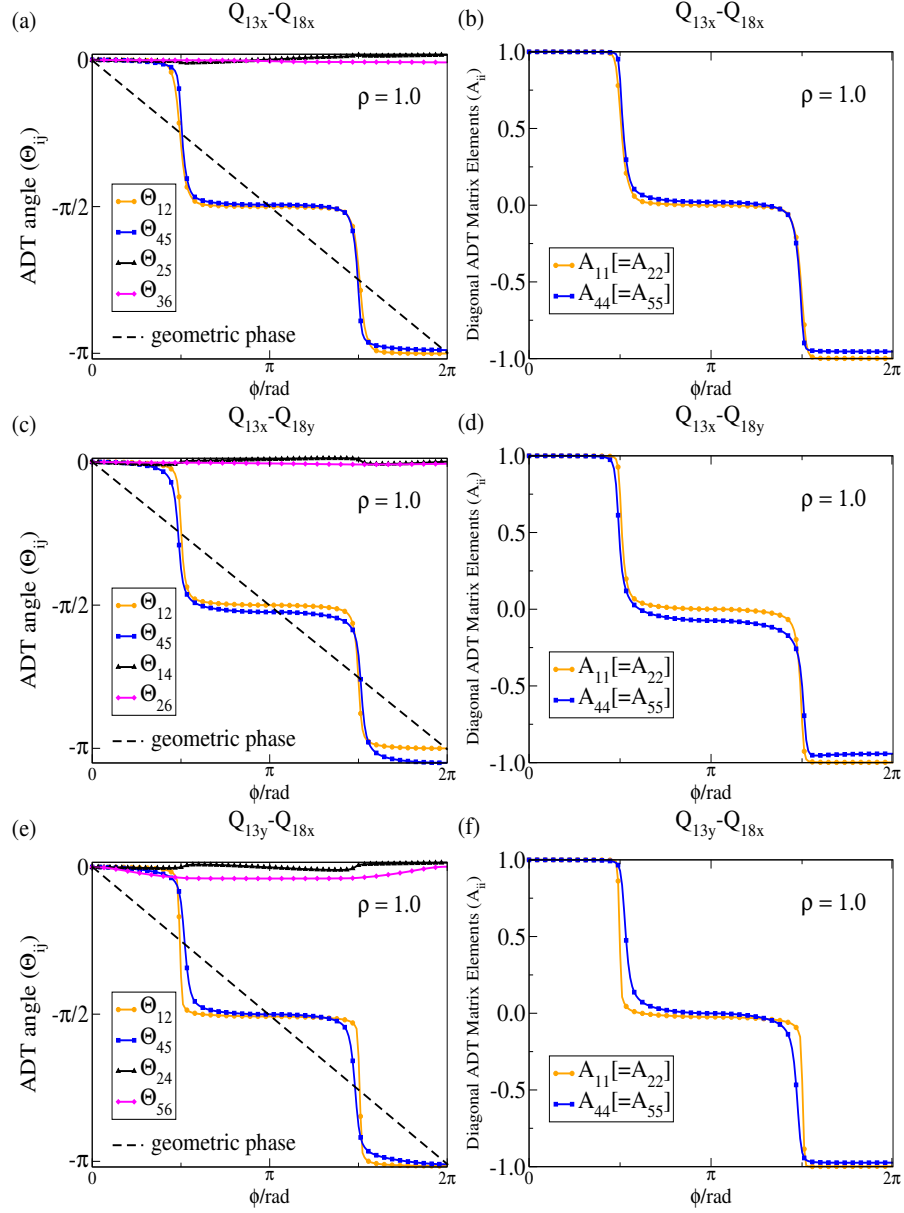


FIG. S28: The left panel depicts 1D cuts of ADT angles, namely, (a) Θ_{12} , Θ_{45} , Θ_{25} and Θ_{36} for $Q_{13x} - Q_{18x}$ pair; (c) Θ_{12} , Θ_{45} , Θ_{14} and Θ_{26} for $Q_{13x} - Q_{18y}$ pair and (e) Θ_{12} , Θ_{45} , Θ_{26} and Θ_{46} for $Q_{13y} - Q_{18x}$ pair along ϕ coordinate at $\rho = 1.0$. The right panel describes 1D functional forms of associated diagonal elements of ADT matrices, viz., $A_{11} [= A_{22}]$ and $A_{44} [= A_{55}]$ for (b) $Q_{13x} - Q_{18x}$, (d) $Q_{13x} - Q_{18y}$ and (f) $Q_{13y} - Q_{18x}$ pairs along the ϕ coordinate at $\rho = 1.0$. The ADT angles representing “1-2” and “4-5” JT/accidental seams attain the value of π at the end of the contour ($\phi = 2\pi$) and the diagonal elements of the ADT matrices exhibit one sign inversion.

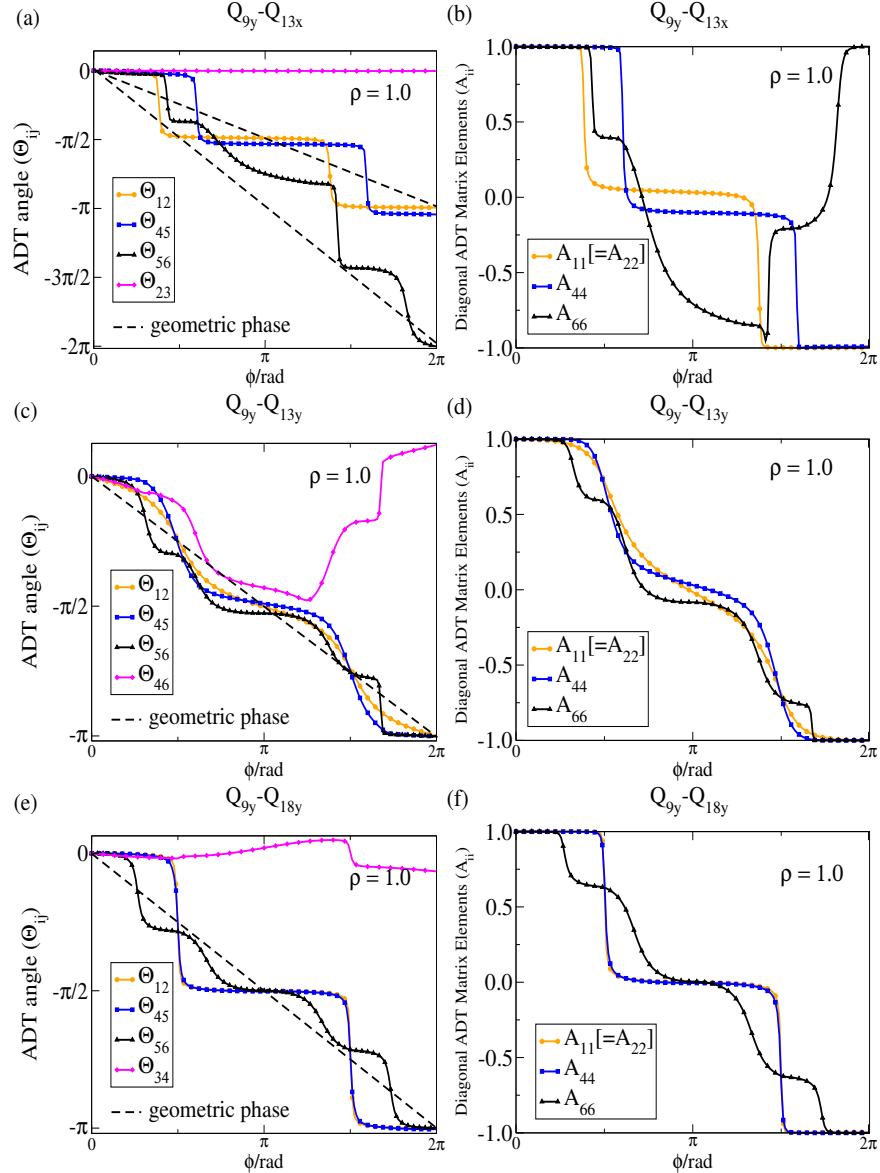


FIG. S29: The figure presents 1D cuts of ADT angles, namely, (a) Θ_{12} , Θ_{45} , Θ_{56} and Θ_{23} for $Q_{9y} - Q_{13x}$ plane; (c) Θ_{12} , Θ_{45} , Θ_{56} and Θ_{46} for $Q_{9y} - Q_{13y}$ plane and (e) Θ_{12} , Θ_{45} , Θ_{56} and Θ_{34} for $Q_{9y} - Q_{18y}$ plane along ϕ coordinate at a specific value of ρ ($= 1.0$). 1D functional forms of the corresponding diagonal elements of ADT matrices, viz., A_{11} [$= A_{22}$], A_{44} and A_{66} for (b) $Q_{9y} - Q_{13x}$, (d) $Q_{9y} - Q_{13y}$ and (f) $Q_{9y} - Q_{18y}$ nuclear CSs are displayed along the ϕ coordinate at ρ ($= 1.0$). The ADT angles associated with “1-2” and “4-5” JT/accidental seams attain the value of π at the end of the contour ($\phi = 2\pi$) and the diagonal elements of the ADT matrices exhibit one sign inversion. On the other hand, Θ_{56} reaches the value of 2π for the first case and π for the other cases for two (2) and one (1) “5-6” seams, respectively. Moreover, A_{66} undergoes necessary sign changes.

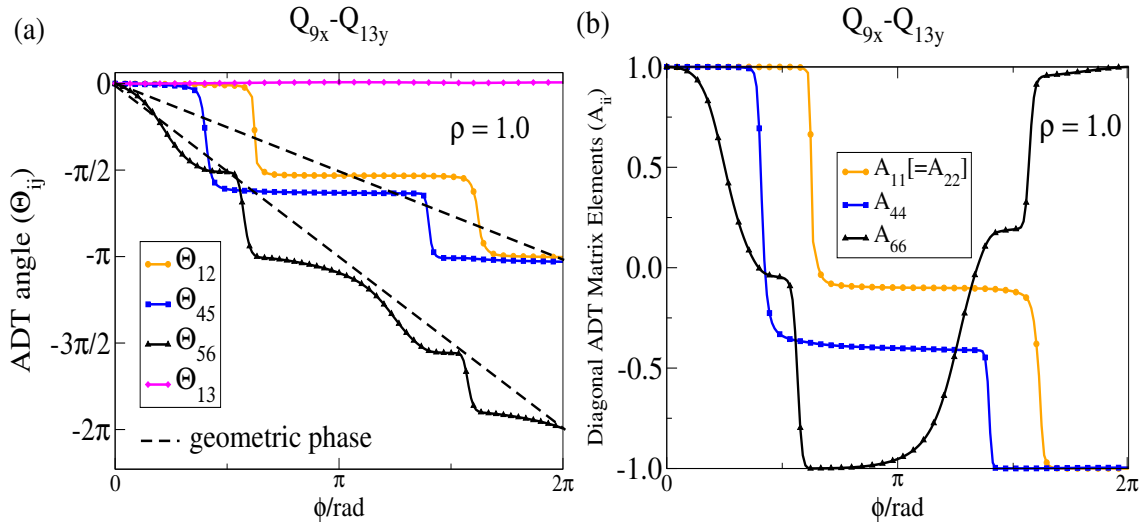


FIG. S30: The left column presents 1D cuts of ADT angles, namely, (a) Θ_{12} , Θ_{45} , Θ_{56} and Θ_{13} for $Q_{9x} - Q_{13y}$ plane along ϕ coordinate at a fixed value of ρ ($= 1.0$). The associated diagonal elements of ADT matrices, namely, (b) $A_{11} [= A_{22}]$, A_{44} and A_{66} are depicted along the ϕ coordinate at ρ ($= 1.0$). The ADT angles representing “1-2” and “4-5” JT CIs/accidental seams attain the value of π at the end of the contour ($\phi = 2\pi$) and the diagonal elements of the ADT matrices encounter one sign inversion.

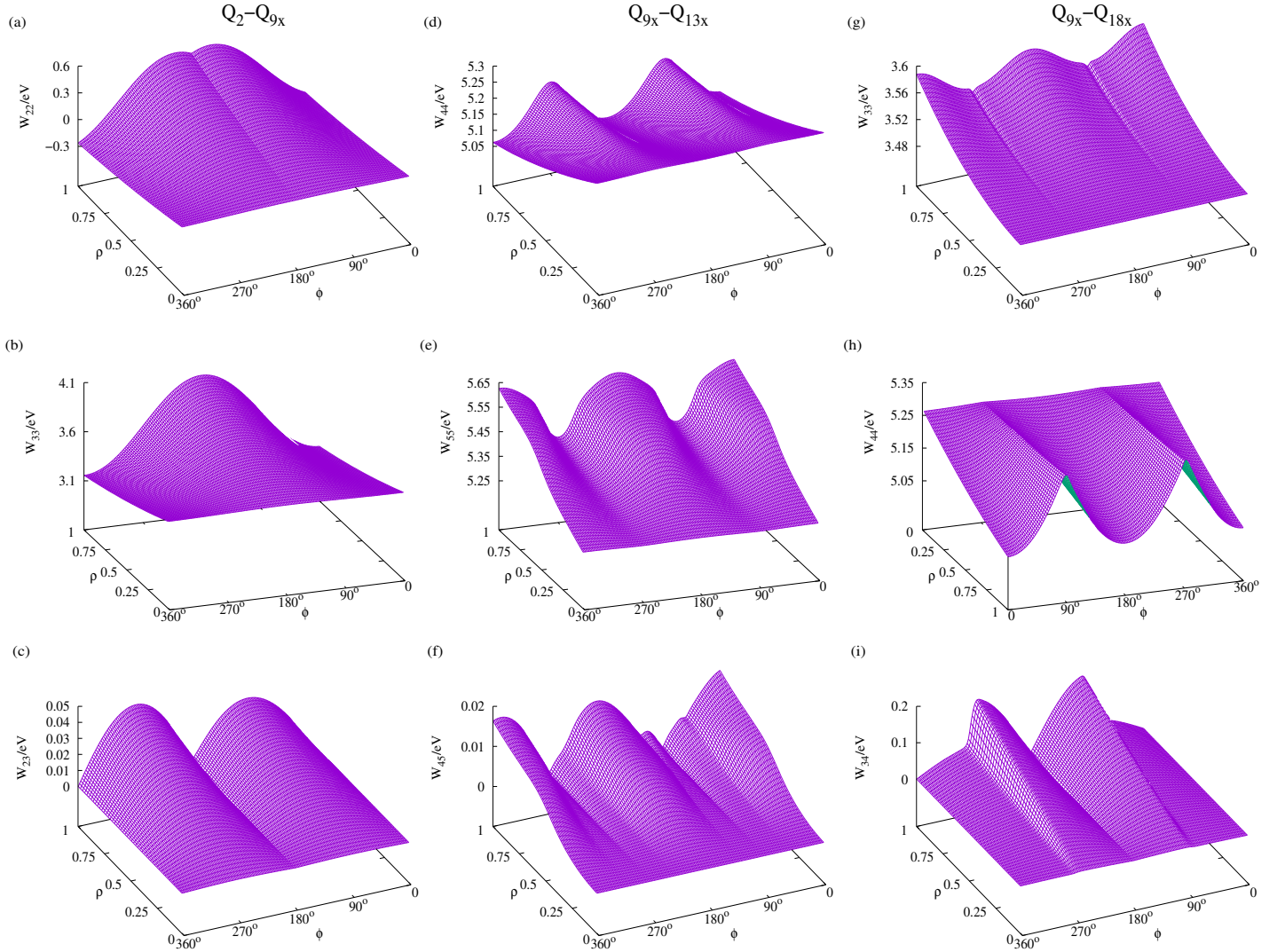


FIG. S31: The diagram displays some representative diabatic PESs and couplings: (a-c) W_{22} , W_{33} and W_{23} for $Q_2 - Q_{9x}$ pair; (d-f) W_{44} , W_{55} and W_{45} for $Q_{9x} - Q_{13x}$ pair; and (g-i) W_{33} , W_{44} and W_{34} for $Q_{9x} - Q_{18x}$ pair. All the diabatic PESs and couplings exhibit smooth, continuous, single-valued functional forms of nuclear coordinates.

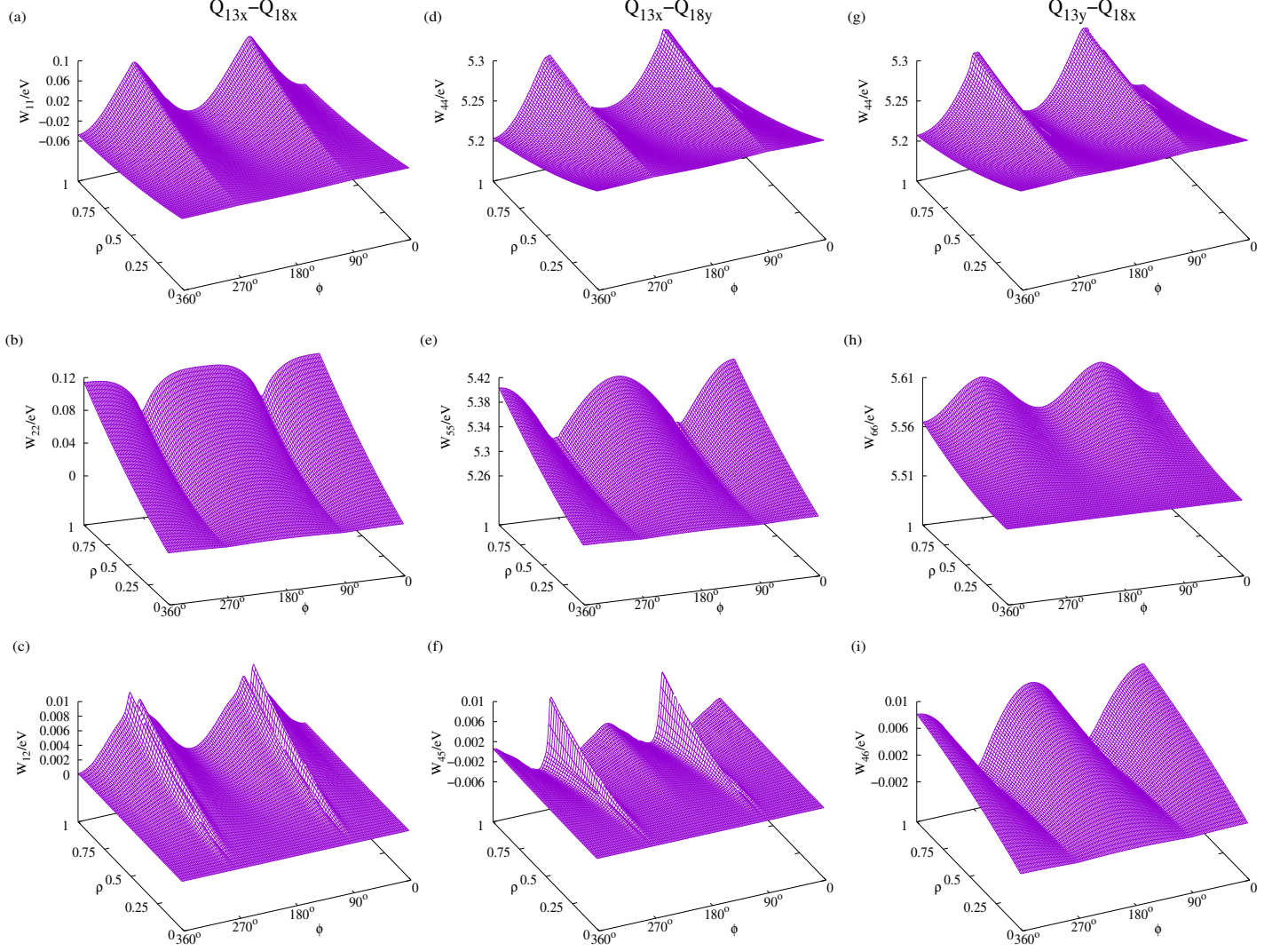


FIG. S32: The diagram presents some representative diabatic PESs and couplings: (a-c) W_{11} , W_{22} and W_{12} for $Q_{13x} - Q_{18x}$ plane; (d-f) W_{44} , W_{55} and W_{45} for $Q_{13x} - Q_{18y}$ plane; and (g-i) W_{44} , W_{66} and W_{46} for $Q_{13y} - Q_{18x}$ plane. The diabatic PESs and couplings appear as well-behaved functions of nuclear coordinates.

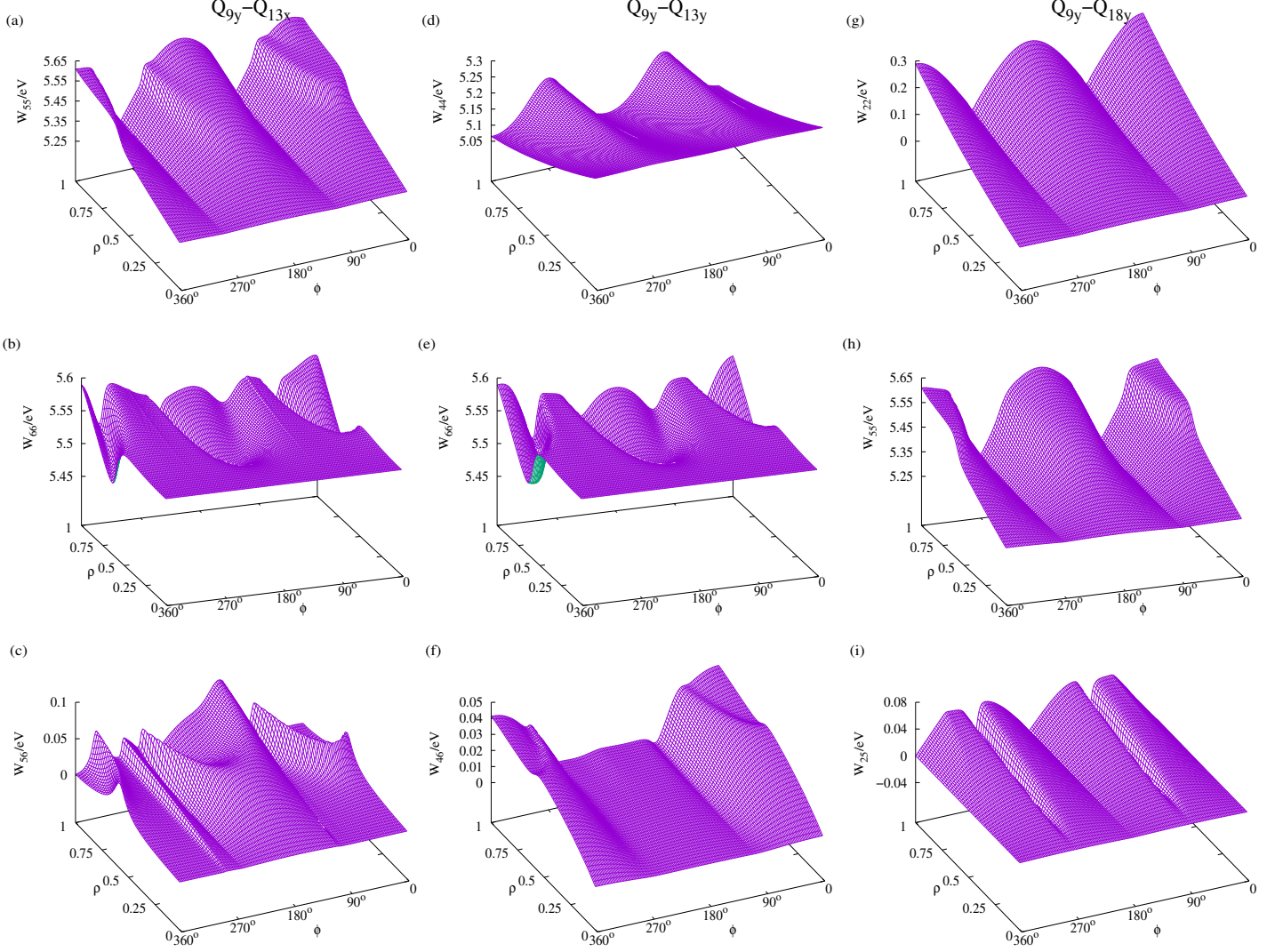


FIG. S33: The diagram shows some representative diabatic PESs and couplings: (a-c) W_{55} , W_{66} and W_{56} for $Q_{9y} - Q_{13x}$ plane; (d-f) W_{44} , W_{66} and W_{46} for $Q_{9y} - Q_{13y}$ plane; and (g-i) W_{22} , W_{55} and W_{25} for $Q_{9y} - Q_{18y}$ plane. The diabatic PESs and couplings appear as smooth, continuous, single-valued functions of nuclear coordinates.

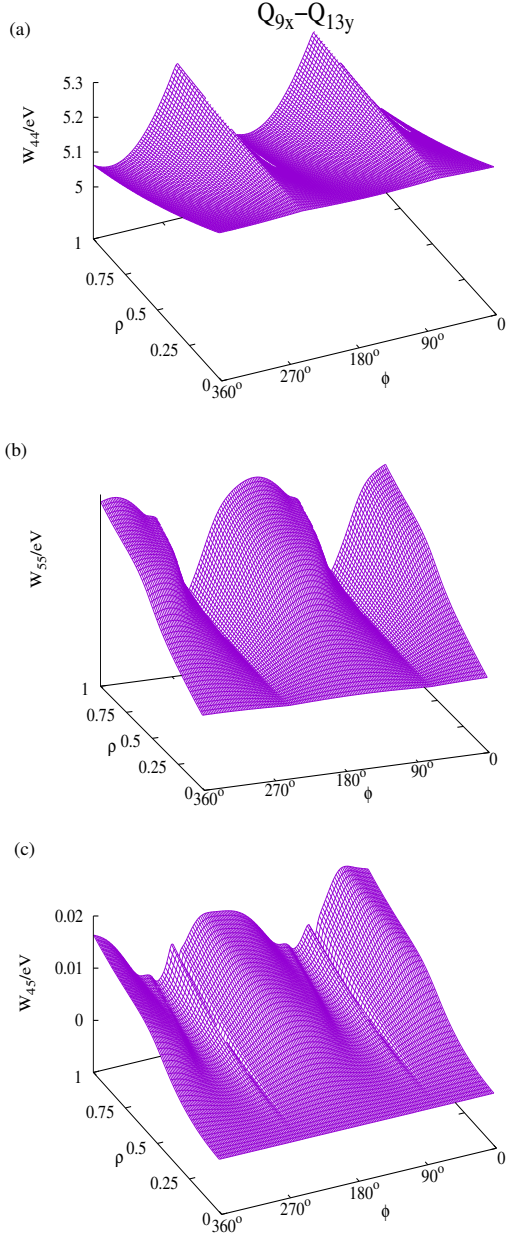


FIG. S34: Some representative diabatic PESs and couplings are presented: (a-c) W_{44} , W_{55} and W_{45} for $Q_{9x} - Q_{13y}$ plane. The functional forms of diabatic PESs and couplings are smooth, continuous and single-valued.

S9 JT Condition : Even Parity Diabatic PESs and Couplings

In the present calculation, the e' normal modes, namely, asymmetric C-C stretching ($Q_{9x} - Q_{9y}$) and C-C-C in-plane bending ($Q_{13x} - Q_{13y}$) are responsible for the JT interactions with doubly degenerate electronic states, \tilde{X}^2E'' and \tilde{B}^2E' , which can be validated using symmetrized direct product analysis for the electronic states (\tilde{X}^2E'' and \tilde{B}^2E') and the e' normal modes (Q_{9x} , Q_{9y} , Q_{13x} and Q_{13y}):

$$E'' \text{ state} \longrightarrow [E'' \times E''] = A'_1 + E'$$

$$E' \text{ state} \longrightarrow [E' \times E'] = A'_1 + E'$$

and

$$e' \text{ mode} \longrightarrow [e' \times e'] = a'_1 + e'$$

On the other hand, while employing the degenerate perturbation theory, the matrix elements for the m th and n th derivatives of vibronic interaction elements along Q_k and Q_l normal modes, respectively can be written as,

$$F_{ij}(Q_k, Q_l) = \sum_{m=0} \sum_{n=0} Q_k^m Q_l^n \left\langle \phi_i^{(0)} \left| \frac{\partial^{(m+n)} W_{ij}(Q_k, Q_l)}{\partial^m Q_k \partial^n Q_l} \right| \phi_j^{(0)} \right\rangle, \quad (25)$$

where i and j are the two electronic states, and W_{ij} represents the Beyond Born Oppenheimer (BBO) constructed diabatic PESs/couplings. In order to verify the JT active feature for each component of those e' degenerate modes (Q_9 and Q_{13}), it is necessary to explore whether the direct product of the integrand in Eq. 25 contains the totally symmetric irreducible representation (IREP):

$$\begin{aligned} & \left[\Gamma(\phi_{E''}^{(0)}) \otimes \Gamma \left(\frac{\partial^{(m+n)} W_{ij}(Q_k, Q_l)}{\partial^m Q_k \partial^n Q_l} \right) \otimes \Gamma(\phi_{E''}^{(0)}) \right] \\ \Rightarrow & \left[\Gamma(E'') \otimes [\Gamma(e')]^{(m+n)} \otimes \Gamma(E'') \right] \in A'_1 \text{ or } a'_1 \end{aligned} \quad (26)$$

$$\begin{aligned} & \left[\Gamma(\phi_{E'}^{(0)}) \otimes \Gamma \left(\frac{\partial^{(m+n)} W_{ij}(Q_k, Q_l)}{\partial^m Q_k \partial^n Q_l} \right) \otimes \Gamma(\phi_{E'}^{(0)}) \right] \\ \Rightarrow & \left[\Gamma(E') \otimes [\Gamma(e')]^{(m+n)} \otimes \Gamma(E') \right] \in A'_1 \text{ or } a'_1 \end{aligned} \quad (27)$$

The integral (see Eq. 25) survives for the JT active normal modes for any order (n and m) of their respective derivatives as per the direct product analysis shown in Eqs. 26 and 27. On the

contrary, if the diabatic PESs or couplings show even-parity functional variation along some specific components, say Q_l (as assumed in Eq. 31 of the main text), the presence of only even power polynomials of Q_l can not be speculated from Eqs. 26 and 27. In other words, if the derivatives of the diabatic PESs/couplings with respect to a particular normal mode for any specific order (m or n) does not exist, the predictability of Eqs. 26 and 27 does not arise. As a matter of fact, the equivalent nuclear configurations generated along positive and negative displacements of a specific normal mode lead to even-parity functional forms of adiabatic PESs and NACTs [see Figs 8(a-c) of main text], which on diabatization also retain such parity in diabatic PESs and couplings [see Figs 8(d-f) of main text].

S10 Schematic Outline of the Degenerate Normal Modes of TFBz⁺

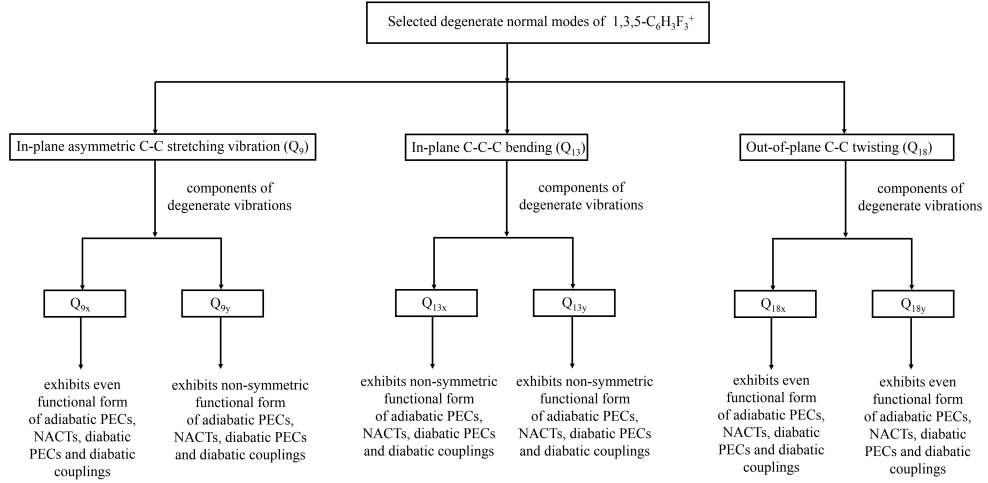


FIG. S35: The diagram depicts a compact description of the chosen degenerate pairs of normal modes.

S11 Even-Parity Diabatic Couplings

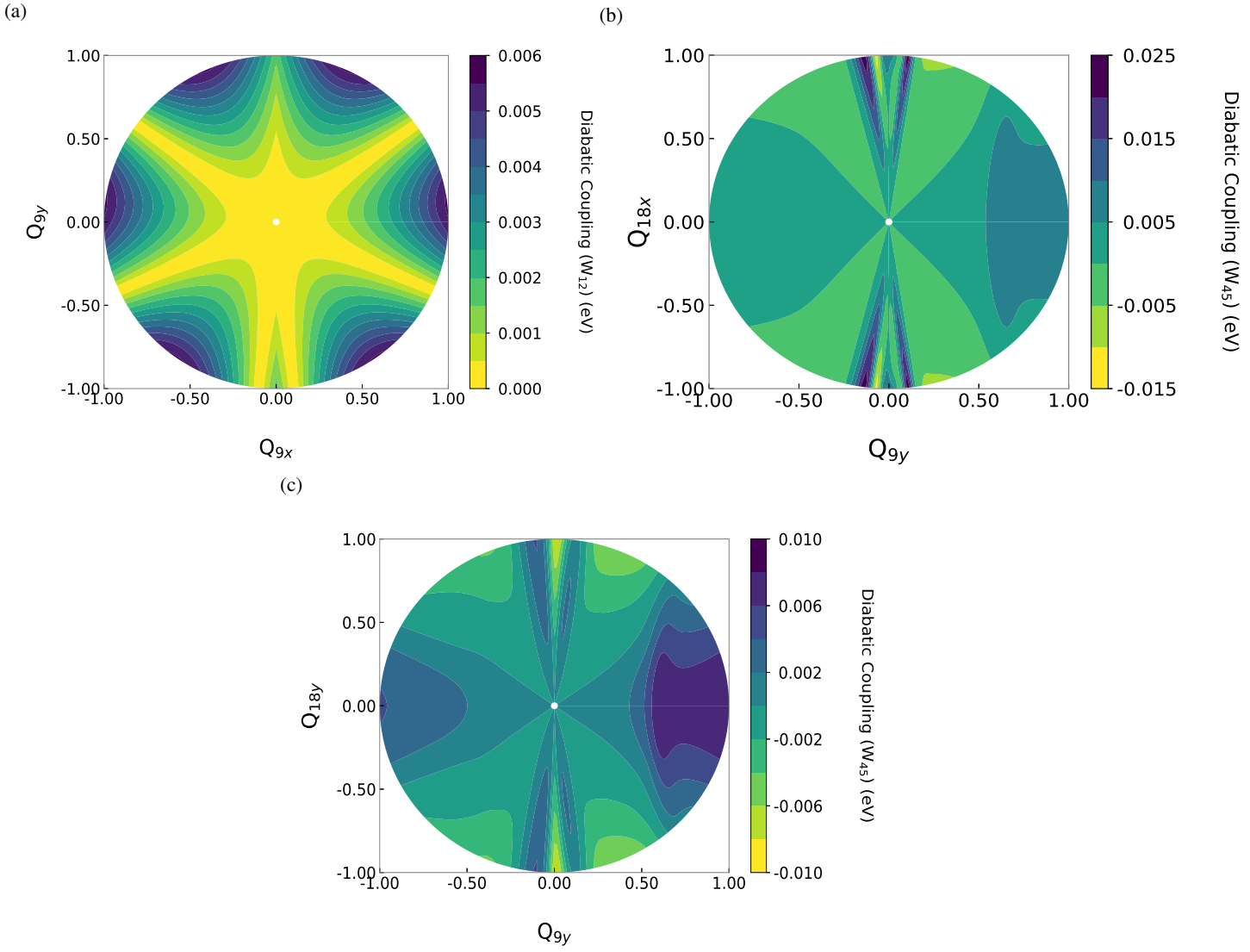


FIG. S36: The figure depicts 2D contour plots of the diabatic coupling elements, (a) W_{12} (\tilde{X}^2E''), (b) W_{45} (\tilde{B}^2E') and (c) W_{45} (\tilde{B}^2E') over $Q_{9x} - Q_{9y}$, $Q_{9y} - Q_{18x}$ and $Q_{9y} - Q_{18y}$ planes, respectively. In each case, the couplings show even-parity functional forms along Q_{9x} , Q_{18x} and Q_{18y} normal modes.

S12 Nuclear Dynamics and Photoelectron (PE) Spectra

S12.1 Convergence of Spectral Profile

TABLE S3: Peak positions of TDDVR calculated spectra [employing BBO based diabatic PESs] for $\tilde{X}^2 E''$ state (ground and first excited states) are presented for four sets of basis functions, where the numbers signify grid points of Q_{13x} , Q_{13y} , Q_{18x} , Q_{18y} , Q_2 , Q_{9x} and Q_{9y} normal modes. The set (13,7,7,5,7,11,13) produces converged spectral profile.

$E(\text{eV})$ (5,5,7,5,7,7,9) 2315250 grid points	$E(\text{eV})$ (7,5,7,5,7,9,11) 5093550 grid points	$E(\text{eV})$ (9,7,7,5,7,11,11) 11205810 grid points	$E(\text{eV})$ (13,7,7,5,7,11,13) 19129110 grid points
9.6371	9.6344	9.6324	9.6324
9.6946	9.6894	9.7212	9.7238
9.7581	9.7466	9.7603	9.7600
9.8087	9.8336	9.8235	9.8233
9.8737	9.8924	9.8702	9.8834
9.9258	9.9264	9.9076	9.9080
9.9660	9.9999	9.9879	9.9895
10.0611	10.0333	10.0541	10.0545

TABLE S4: Peak positions of TDDVR based spectra (using BBO calculated diabatic PESs) for $\tilde{A}^2 A''_2$ state (second excited states) are summarized for four sets of basis functions, where the numbers represent grid points of Q_{13x} , Q_{13y} , Q_{18x} , Q_{18y} , Q_2 , Q_{9x} and Q_{9y} normal modes. The set (13,7,7,5,7,11,13) leads to converged spectral profile.

$E(\text{eV})$ (5,5,7,5,7,7,9) 2315250 grid points	$E(\text{eV})$ (7,5,7,5,7,9,11) 5093550 grid points	$E(\text{eV})$ (9,7,7,5,7,11,11) 11205810 grid points	$E(\text{eV})$ (13,7,7,5,7,11,13) 19129110 grid points
12.3389	12.3371	12.3356	12.3357
12.3950	12.3906	12.3837	12.3814
12.4582	12.4518	12.4450	12.4460
12.5263	12.5138	12.5287	12.5289
12.5755	12.6021	12.5943	12.5927
12.6240	12.6453	12.6420	12.6426
12.6908	12.6886	12.7055	12.7064
12.7857	12.7959	12.7736	12.7764
12.8275	12.8533	12.8138	12.8143

TABLE S5: TDDVR calculated spectral position (obtained from BBO based diabatic PESs) for \tilde{B}^2E' – $\tilde{C}^2A'_2$ state (third to fifth excited states) are depicted for four sets of basis functions, where the numbers indicate grid points of Q_{13x} , Q_{13y} , Q_{18x} , Q_{18y} , Q_2 , Q_{9x} and Q_{9y} normal modes. The set (13,7,7,5,7,11,13) results into converged spectral profile.

$E(\text{eV})$ (5,5,7,5,7,7,9) 2315250 grid points	$E(\text{eV})$ (7,5,7,5,7,9,11) 5093550 grid points	$E(\text{eV})$ (9,7,7,5,7,11,11) 11205810 grid points	$E(\text{eV})$ (13,7,7,5,7,11,13) 19129110 grid points
13.4259	13.4006	13.3890	13.3870

S12.2 PE spectra Including and Excluding Q_2 Normal Mode

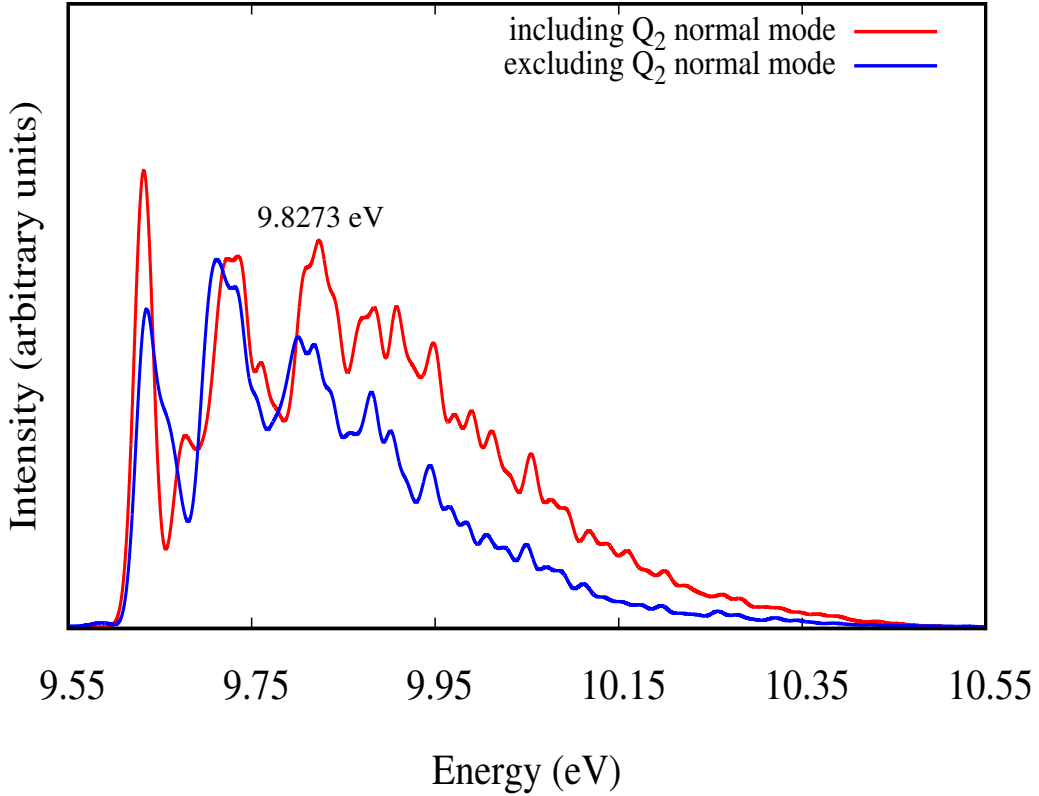


FIG. S37: The diagram depicts PE spectra for \tilde{X}^2E'' state obtained from TDDVR formalism using BBO based diabatic PESs and couplings in (a) presence [(13,7,7,5,7,11,13) basis set with 19129110 number of grid points] and (b) absence [(13,7,7,5,11,13) basis set with 2732730 number of grid points] of Q_2 normal mode (C-F symmetric stretching). While excluding the Q_2 mode, the intensity of spectral peak at 9.8273 eV diminishes as well as gets broadened affirming the importance of C-F symmetric stretching.

S12.3 PE Spectra Including Additional Modes

\tilde{X}^2E'' State

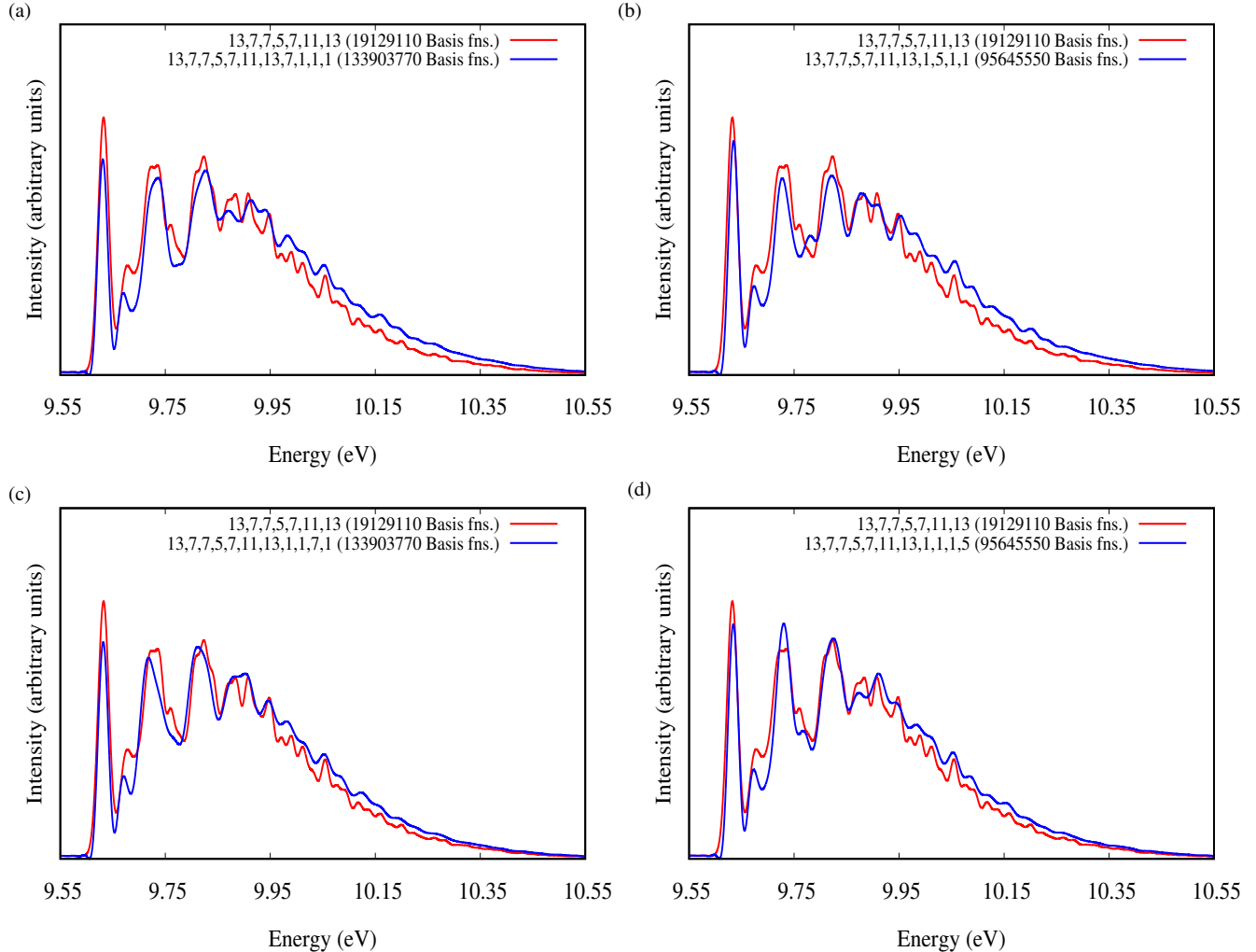


FIG. S38: The diagram displays the comparison of theoretically calculated spectra by TDDVR methodology over BBO based diabatic PESs for the lower basis set $(13,7,7,5,7,11,13)$ with the larger ones, namely, (a) $(13,7,7,5,7,11,13,7,1,1,1)$, (b) $(13,7,7,5,7,11,13,1,5,1,1)$, (c) $(13,7,7,5,7,11,13,1,1,7,1)$ and (d) $(13,7,7,5,7,11,13,1,1,1,5)$ for \tilde{X}^2E'' state. The additional four numbers in the sets represent the grid points of Q_{10x} , Q_{10y} , Q_{12x} and Q_{12y} , respectively. While including (a) Q_{10x} , (b) Q_{10y} , (c) Q_{12x} and (d) Q_{12y} modes as “quantum” modes in the dynamical calculation, the spectral profile remains almost invariant. For each cases, the remaining three modes act as “classical” modes.

$\tilde{A}^2 A''_2$ State

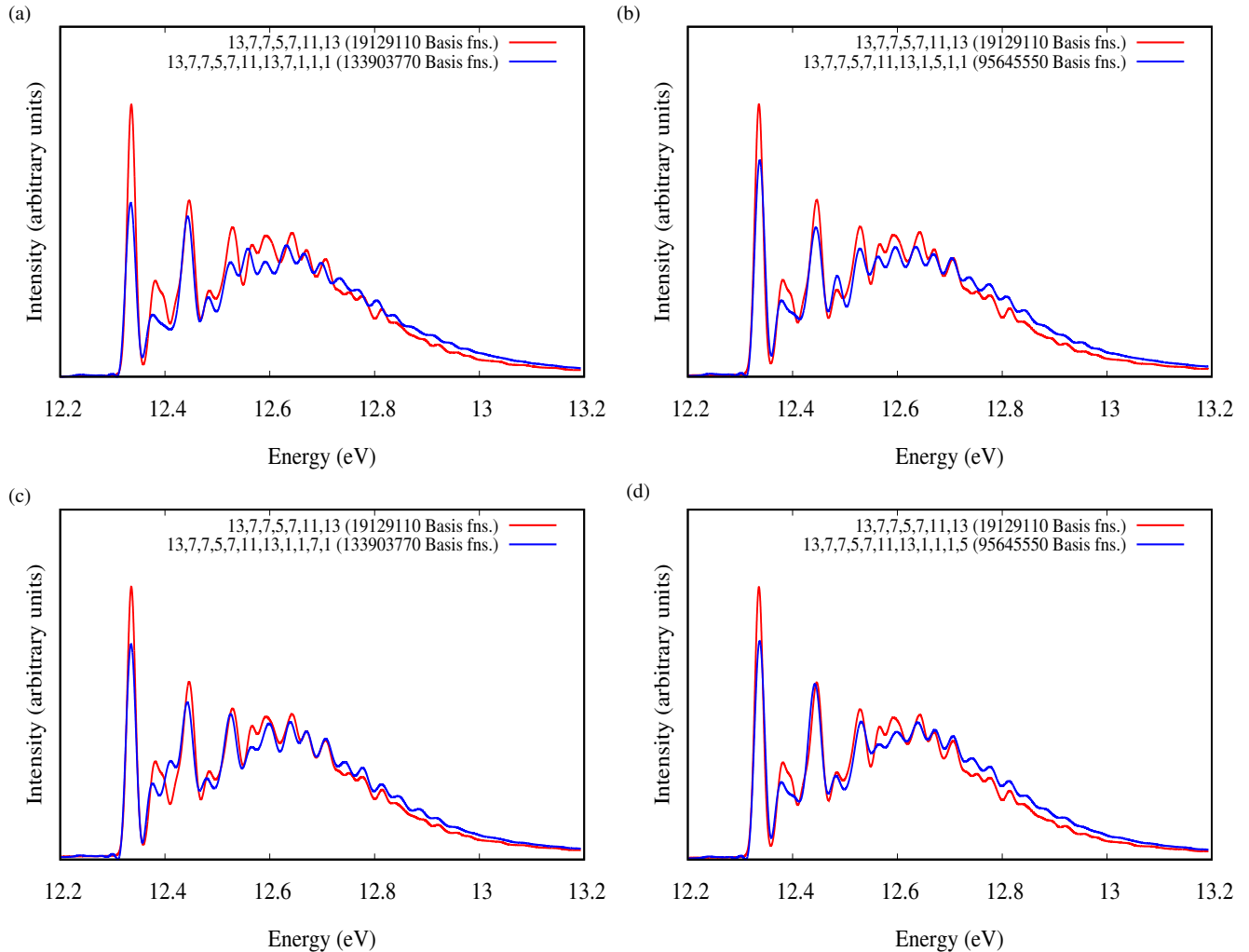


FIG. S39: The diagram depicts theoretical spectral profile obtained from TDDVR methodology using BBO calculated diabatic PESs for the lower basis set ($13,7,7,5,7,11,13$) and its comparison with larger ones, namely (a) ($13,7,7,5,7,11,13,7,1,1,1$), (b) ($13,7,7,5,7,11,13,1,5,1,1$), (c) ($13,7,7,5,7,11,13,1,1,7,1$) and (d) ($13,7,7,5,7,11,13,1,1,1,5$) for $\tilde{A}^2 A''_2$ state. If (a) Q_{10x} , (b) Q_{10y} , (c) Q_{12x} and (d) Q_{12y} modes are included as “quantum” modes in the dynamical calculation, no significant changes are observed in the spectral profile. In each case, the rest of the three modes are treated as “classical” modes.

$\tilde{B}^2E' - \tilde{C}^2A'_2$ States

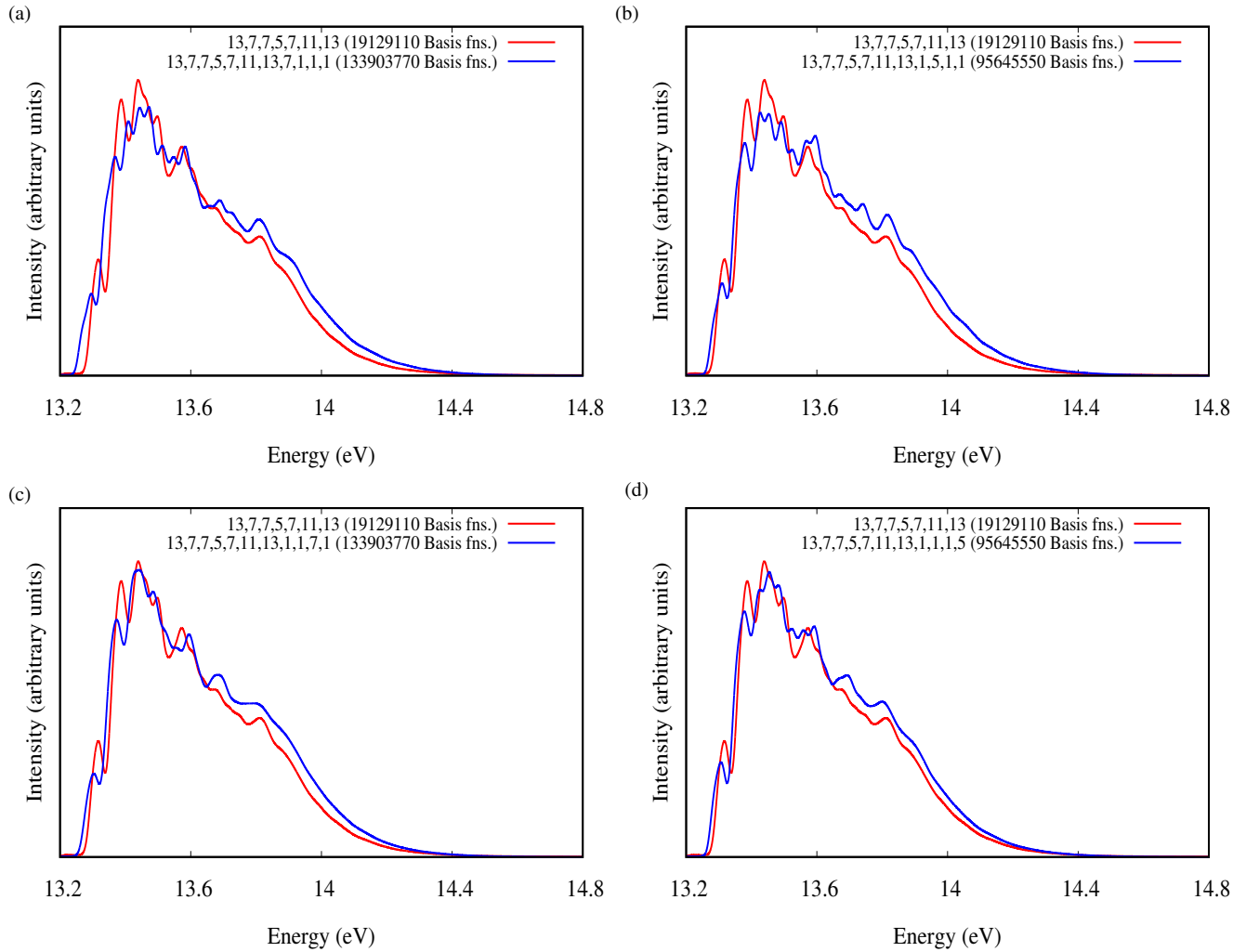


FIG. S40: The diagram demonstrates theoretically calculated spectra obtained from TDDVR methodology employing BBO computed diabatic PESs for the lower basis set ($13,7,7,5,7,11,13$) and its comparison with larger ones, namely (a) ($13,7,7,5,7,11,13,7,1,1,1$), (b) ($13,7,7,5,7,11,13,1,5,1,1$), (c) ($13,7,7,5,7,11,13,1,1,7,1$) and (d) ($13,7,7,5,7,11,13,1,1,1,5$) for $\tilde{B}^2E' - \tilde{C}^2A'_2$ states. If (a) Q_{10x} , (b) Q_{10y} , (c) Q_{12x} and (d) Q_{12y} modes are incorporated as “quantum” modes in the dynamical calculation, minimal changes are observed in the spectral envelop. In each case, the rest of the three modes behave as “classical” modes.

S12.4 Comparison of PE Spectra Calculated from TDDVR and Fast Fourier Transformation (FFT) - Lanczos Methods

In this subsection, we compare the PE spectra of TFBz using FFT-Lanczos dynamics over BBO based diabatic PESs ($\sim 1.26 \times 10^7$ number of grid points) with fully converged TDDVR profiles using same BBO based diabatic surfaces ($\sim 1.32 \times 10^7$ number of basis functions) as well as with the experimental findings.¹³ Fig. S37 and Table S6 display that few peaks in the experimental spectral bands¹³ (9.8917 eV, 10.0642 eV for \tilde{X}^2E'' and 12.5849 eV for \tilde{A}^2A_2'' states) are missing in the theoretical ones obtained from FFT-Lanczos dynamics. In addition, some (FFT-Lanczos) peaks (9.7804 eV, 9.9728 eV for \tilde{X}^2E'' and 12.4214 eV, 12.7202 eV for \tilde{A}^2A_2'' states) are substantially shifted from their corresponding experimental counterpart¹³ (9.7696 eV, 9.9939 eV, 12.4031 eV and 12.7056 eV). Moreover, the diffused spectral patterns for \tilde{X}^2E'' and \tilde{A}^2A_2'' states¹³ (at > 10.0 eV and > 12.7 eV) originating from the overtones of various vibrational frequencies are absent in the FFT-Lanczos based spectra. Finally, the intensity of the peaks also show wide difference from the experimentally findings.¹³ Nevertheless, the TDDVR calculated spectra exhibit peak by peak correspondence, which justifies better applicability of such algorithm for large molecular systems like TFBz.

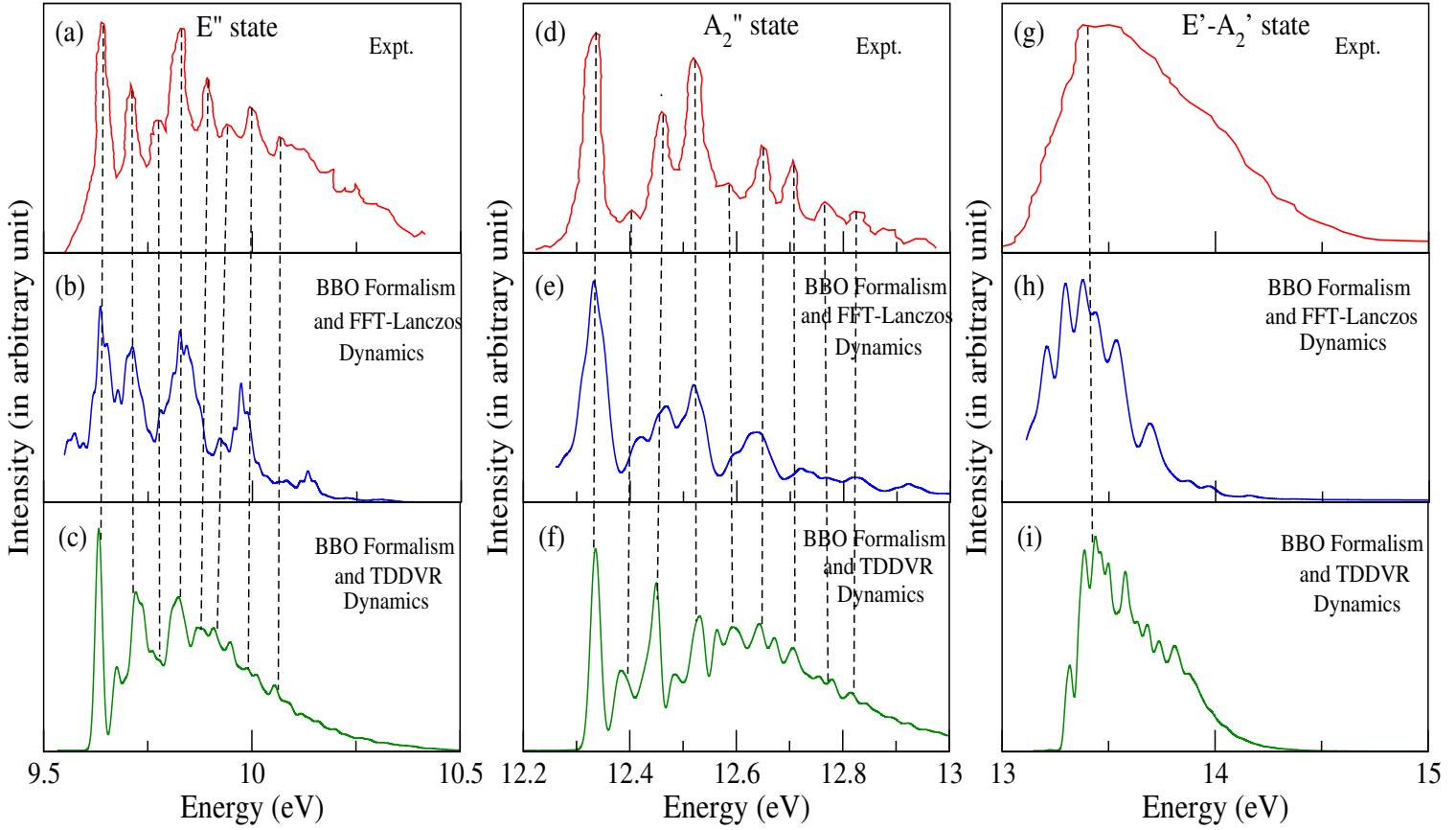


FIG. S41: The left panel shows (a) experimental PE spectrum of TFBz¹³ for the ground degenerate state (\tilde{X}^2E'') in comparison with the theoretical spectra obtained from (b) FFT-Lanczos methodology on BBO based diabatic surfaces¹⁰ and from (c) TDDVR methodology on the same diabatic PESs. The middle (d-f) and the right (g-i) columns depict the same quantities for \tilde{A}^2A_2'' and $\tilde{B}^2E' - \tilde{C}^2A_2'$ states, respectively. For all the three cases, TDDVR calculated spectra exhibit better peak by peak correspondence with the experimental¹³ ones.

TABLE S6: Comparison of peak positions among experimental spectra¹³ and theoretical spectra obtained from BBO based diabatic Hamiltonian (using FFT-Lanczos and TDDVR dynamics) for \tilde{X}^2E'' , \tilde{A}^2A_2'' and $\tilde{B}^2E' - \tilde{C}^2A_2'$ states is presented.

\tilde{X}^2E'' state			\tilde{A}^2A_2'' state			$\tilde{B}^2E' - \tilde{C}^2A_2'$ states		
E (eV) (experiment of Gilbert <i>et al.</i> ¹³)	E (eV) (FFT-Lanczos)	E (eV) (TDDVR)	E (eV) (experiment of Gilbert <i>et al.</i> ¹³)	E (eV) (FFT-Lanczos)	E (eV) (TDDVR)	E (eV) (experiment of Gilbert <i>et al.</i> ¹³)	E (eV) (FFT-Lanczos)	E (eV) (TDDVR)
9.6383	9.6359	9.6324	12.3356	12.3321	12.3356	13.3772	13.3780	13.3866
9.7086	9.7125	9.7212	12.4031	12.4214	12.3838			
9.7696	9.7804	9.7603	12.4595	12.4678	12.4496			
9.8281	9.8266	9.8235	12.5189	12.5194	12.5310			
9.8917	—	9.8702	12.5849	—	12.5933			
9.9382	9.9222	9.9076	12.6461	12.6385	12.6431			
9.9939	9.9728	9.9879	12.7056	12.7202	12.7063			
10.0642	—	10.0541	12.7651	12.7675	12.7794			
			12.8198	12.8201	12.8150			

References

- [1] S. Mukherjee, J. Dutta, B. Mukherjee, S. Sardar, and S. Adhikari, *J. Chem. Phys.* **150**, 064308 (2019).
- [2] S. Mukherjee, S. Bandyopadhyay, A. K. Paul, and S. Adhikari, *J. Phys. Chem. A* **117**, 3475 (2013).
- [3] J. Dutta, S. Mukherjee, K. Naskar, S. Ghosh, B. Mukherjee, S. Ravi, and S. Adhikari, *Phys. Chem. Chem. Phys. (Perspective)* **22**, 27496 (2020).
- [4] S. Mukherjee, S. Ravi, K. Naskar, S. Sardar, and S. Adhikari, *J. Chem. Phys.* **154**, 094306 (2021).
- [5] K. Naskar, S. Mukherjee, B. Mukherjee, S. Ravi, S. Mukherjee, S. Sardar, and S. Adhikari, *J. Chem. Theory Comput.*, see <https://pubs.acs.org/doi/10.1021/acs.jctc.9b00948> or <https://github.com/AdhikariLAB/ADT-Program> **16**, 1666 (2020).
- [6] B. Mukherjee, K. Naskar, S. Mukherjee, S. Ghosh, T. Sahoo, and S. Adhikari, *Int. Rev. Phys. Chem.* **38**, 287 (2019).
- [7] S. Mandal, S. Ghosh, S. Sardar, and S. Adhikari, *Int. Rev. Phys. Chem.* **37**, 607 (2019).
- [8] P. A. M. Dirac, *Proc. Cambridge philos. Soc.* **26**, 376 (1930).
- [9] P. Puzari and S. Adhikari, *Int. J. Quant. Chem.* **98**, 434 (2004).
- [10] T. Mondal and S. Mahapatra, *Phys. Chem. Chem. Phys.* **11**, 10867 (2009).
- [11] F. Ramondo, G. Portalone, A. Domenicano, G. Schultz, and I. Hargittai, *J. Mol. Struct.* **269**, 367 (1992).
- [12] D. A. Braden and B. S. Hudson, *J. Phys. Chem. A* **104**, 982 (2000).
- [13] R. Gilbert, P. Sauvageau, and C. Sandorfy, *Chem. Phys. Lett.* **17**, 465 (1972).